MODELING AND CHARACTERIZATION OF BIPOLAR DEVICES

BY

JONG-SIK PARK

A DISSERTATION PRESENTED TO THE GRADUATE SCHOOL OF
THE UNIVERSITY OF FLORIDA
IN PARTIAL FULFILMENT OF THE REQUIREMENTS FOR THE
DEGREE OF DOCTOR OF PHILOSOPHY

UNIVERSITY OF FLORIDA

1987

TO MY GRANDMOTHER

ACKNOWLEDGMENTS

I wish to express my sincere appreciation to the chairman of my supervisory committee, Professor Arnost Neugroschel, and the co-chairman, Professor Fredrik A. Lindholm, for their guidance, encouragement, and support throughout the course of this work. I also thank Professors Sheng S. Li, Gys Bosman, and Hendrik Jan Monkhorst for their participation on my supervisory committee.

I am grateful to Dr. Denny D. Tang of IBM Thomas J. Watson Research Center for advising the analysis of the lateral p-n-p transistor.

I want to express my appreciation to Drs. Hyung-Gyu Lim, Tae-Won Jung, and Mrs. Konstantinos Misiakos, Ju-Sung Park, Hanggeun Jeong, and Chung-Gyun Choi for many helpful discussions.

I am indebted to my wife, Jinna, for her support and patience during all the years of this study.

The financial support of the Semiconductor Research Corporation, National Science Foundation, and the Jet Propulsion Laboratory are gratefully acknowledged.

TABLE OF CONTENTS

Page

ACKNOWLEDGEMENTS iii

ABSTRACT.....vi

CHAPTER

ONE INTRODUCTION.....1

TWO SYSTEMATIC ANALYTICAL SOLUTIONS FOR MINORITY-CARRIER TRANSPORT IN SEMICONDUCTORS WITH POSITION DEPENDENT COMPOSITION, WITH APPLICATION TO HEAVILY-DOPED SILICON.....5

2.1 Introduction.....5
2.2 Theory.....8
2.2.1 Transport Equations in Quasi-Neutral Region....8
2.2.2 Integral Representation of the Analytical Solution.....11
2.2.3 Approximation of the Solution by Truncating at Finite order.....15
2.3 Comparison of the Truncated Solutions with Computer Results.....22
2.4 Conclusions.....30

THREE DETERMINATION OF BANDGAP NARROWING FROM ACTIVATION PLOTS..32

3.1 Introduction.....32
3.2 A Simple Theory for the Interpretation of Experimental Results.....33
3.3 Experimental Results and Discussions.....35
3.4 Conclusions.....37

FOUR PHYSICS AND NUMERICAL METHODS ON THE MINORITY-CARRIER TRANSPORT IN THE QUASI-NEUTRAL REGION UNDER SMALL SIGNAL EXCITATIONS.....39

4.1 Introduction.....39
4.2 Small-Signal Transport Equations and Numerical Method.....40
4.2.1 Small Signal Transport Equations.....40
4.2.2 Numerical Method.....43
4.3 Numerical Results and Discussions.....45
4.4 Summary.....67

CHAPTER

FIVE AN ANALYTICAL STUDY OF THE P/N JUNCTION SPACE-CHARGE REGION UNDER HIGH FORWARD VOLTAGE....69

5.1 Introduction....69
5.2 Basic Concepts....71
5.3 Symmetric Step Junction Under High Forward Voltage....77
5.4 Exponential Profile and Linearly Graded Junction....83
5.5 Discussion....89

SIX STUDY OF THE LAREAL P-N-P TRANSISTORS USING TWO DIMENSIONAL DEVICE SIMULATOR....95

6.1 Introduction....95
6.2 Analysis....95
6.3 Summary....106

SEVEN SUMMARY....108

APPENDICES

A SIMPLE ESTAMATION OF THE QUASI-NEUTRAL QUASI-EQUILIBRIUM CONDITION....110

B CALCULATION OF Q_E, C_E, AND τ_E FOR THE ZEROTH-ORDER APPROXIMATION....112

REFERENCES....114

BIOGRAPHICAL SKETCH....120

Abstract of the Dissertation Presented to the Graduate School
of the University of Florida in Partial Fulfillment of the
Requirements for the Degree of Doctor of Philisophy

MODELING AND CHARACTERIZATION OF
BIPOLAR DECICES

By

Jong-Sik Park

April 1987

Chairman: Arnost Neugroschel
Cochairman: Fredrik A. Lindholm
Major Department: Electrical Engineering

This dissertation describes the modeling and characterization of bipolar devices.

Heavy doping parameters such as bandgap narrowing and diffusion length, which are crucial to the design and characterization of modern bipolar devices, are determined by measuring the base saturation currents of bipolar transistors with same doping profile but with different emitter surface contacts, ohmic and polysilicon contacts. This method has the advantage of avoiding questionable assumptions on the value and temperature dependence of the minority-carrier diffusion coefficient.

Transport of minority-carriers inside the quasi-neutral region is solved based on the new concept of the quasi-neutral quasi-equilibrium condition. The base current by the transport of injected minority holes into the neutral region can be predicted and approximated by truncating the general solution.

A numerical method that solves the small-signal transport equations in the quasi-neutral region is developed. Based on this method a computer program is written and the simulation results are interpreted physically. The degradation of high-frequency performance of bipolar transistores caused by small-signal transport in the neutral region is discussed based on the numerical results.

For the complete modeling of the space-charge region capacitance the analytical solutions of the space-charge region under high forward voltage, in which range the depletion approximation cannot be applied, are developed. The results agree well with the numerical simulation results.

The characteristics of the lateral p-n-p transistors are studied using the two dimensional device simulator. DC current gain and the base charge storage time for different geometries and doping profiles are studied and the design principles for fabricating fast lateral p-n-p transistors together with vertical n-p-n transistors are developed.

CHAPTER ONE
INTRODUCTION

Since the invention of the bipolar transistor in 1946 and the development of semiconductor device theory by Shockley [1], the performance of bipolar transistors has been improved with the advances in the device fabrication technology. Recently, the scaling-down of the device size using self-alignment technology [2] enables the reduction of the device size and the improvement of the AC and transient device performances.

Bipolar scaling theory [3,4] predicts that the scaling of the device has to be done in both lateral and vertical directions. For the scaling in the vertical direction the active base region has to be kept narrow. But to maintain the active quasi-neutral base region the doping concentration has to be increased with the scaling-down of the device. As the doping concentration reaches 2 x 18 cm^{-3} in silicon, overlap occurs between the valence electrons of the impurity atoms and the semi-classical device theory based on the free carrier approximation cannot accurately predict the device performance. Some of the heavy doping effects are

(a) bandgap shrinkage: as the interactions between the carriers become larger, carriers distribute themselves to reduce the self-energy of the system and the bandgap narrowing occurs. Since the minority carriers are generated by thermal

excitation, the main effect of the bandgap narrowing is the increased minority carrier concentration;

(b) Auger recombination: as the concentration of carriers is increased, more hot carriers are generated and the recombination via these hot carriers reduces the minority carrier lifetime than anticipated by the SRH theory;

(c) minority carrier diffusion coefficient: as the doping level is increased, the minority carrier diffusion coefficient becomes different from that of the majority carrier because of trapping into the localized band-tail states, difference of the scattering cross section between the attractive and repulsive interaction between carriers and the impurity atoms, and the carrier-carrier interaction. The minority carrier diffusion coefficient is crucial in predicting the speed of the device.

One of the promising methods to achieve lateral scaling is the use of polysilicon as an emitter diffusion source and emitter contact. Experimental results [5-7] show that the of the minority carriers are blocked inside the single crystal silicon layer when it is contacted with the polysilicon and the reflection properties of the polysilicon contact can be modeled with the effective surface recombination velocity at the mono-poly silicon interface.

In this dissertation we try to make contributions to the understanding of modern bipolar devices.

In Chapter Two we discuss the transport of the minority-carriers inside the heavily doped quasi-neutral region. Based on the formation

of the quasi-equilibrium condition inside the neutral region, we develop a general solution for the spatial distributions of the current and minority carriers. When the general solution for the heavily doped emitter region is truncated, we can get analytical solutions with any order of accuracy, some of which are identical to the approximations that appear elsewhere. The most simple approximation, the quasi-neutral quasi-equilibrium approximation (QNQE), is accurate enough for transitors with poly-diffused emitters and solar cells.

In Chapter Three we present the measurements of bandgap narrowing and the minority-carrier diffusion length in the heavily doped region. For the measurement of the diffusion length, we compare the base saturation current of two transistors with the same doping profile but with different emitter surface contacts. Bandgap shrinkage is determined by measuring the temperature dependence of base saturation current for bipolar transistors with polysilicon emitter contacts. This measurement method has the advantage of avoiding the assumptions for the questionable value and temperature dependence of the minority-carrier diffusion coefficient.

Chapter Four describes the physics and numerical methods of the AC small signal transport in the quasi-neutral region. Exploiting the linearity of the AC transport equations, we develop a simple numerical algorithm that enables a simulation of AC transport equations numerically. Compared to the other AC small signal device simulators that need much more memory space and excution time, our program can be written for any small personal computer and has the advantage of affording a physical insight useful for the design of fast bipolar transistors. From the analysis of the simulation results we conclude

that the origin of the difference between the small signal capacitance and the quasi-static capacitance can be interpretated as the breakdown of the quasi-equilibrium condition inside the neutral region and that the DC simulation results for the transition region capacitance are nearly equal to the AC small signal capacitance. Therefore a complete small signal equivalent circuit can be build by combining the DC simulation results for the transition region and the small signal simulation results inside the neutral region.

We develop in Chapter Five analytical solutions for the behavior of the transition region under high forward bias voltage where the depletion approximation cannot be applied. For the comparison with the numerical results we wrote a computer program that solves the Poisson equation inside the transition region and the comparison shows good agreement at high forward bias voltage range.

In Chapter Six we study the characteristics of the scaled lateral p-n-p transistors using the two dimensional device simulator (FIELDAY). Simple analytical approximations for the base current and the collector current agree well with the numerical results. For the prediction of the transient response we simulate the base charge storage time, which leads to the qualitative understanding of the procedures for the design of fast lateral p-n-p transistors.

CHAPTER TWO

SYSTEMATIC ANALYTICAL SOLUTIONS FOR MINORITY CARRIER TRANSPORT IN SEMICONDUCTORS WITH POSITION-DEPENDENT COMPOSITION, WITH APPLICATION TO HEAVILY-DOPED SILICON

2.1 Introduction

As the understanding of heavily doped semiconductors has gradually evolved, the transport phenomena of minority carriers injected into heavily doped emitters and the other regions of semiconductor devices have been extensively studied. For a nonuniformly doped emitter, heavy doping effects, such as bandgap narrowing, Auger lifetime, and minority carrier diffusion coefficient, are all position dependent. Thus an intuitive understanding of the minority-carrier transport phenomena becomes complicated. Even though exact numerical solutions can be obtained from a computer simulation, an analytical approximation is useful for determining design principles and providing physical insight.

Many efforts have sought a simple analytical approximation. Dumke [8] derived a Hermite polynomial expression for a gaussian doping profile. He assumed that diffusion dominates the minority-carrier current and the diffusion coefficient is independent of doping. De Graaf et al. [9] incorporated bandgap narrowing, doping-dependent Auger lifetime, built-in electric field, and finite surface recombination velocity S at the emitter contact. They divided the emitter into two subregions (field dominant and diffusion dominant), in which analytical

expressions were derived based on computer simulation. Amantea [10] also divided the emitter into field- and diffusion-dominant regions. He pointed out that the transport equation that looks like a boundary-value problem can be solved as an initial value problem that avoids the iteration methods needed in a computer solution. Shibib et al.[11] included majority carrier degeneracy and finite surface recombination velocity at the emitter surface in a transparent emitter model for thin emitters, where the emitter transit time is much smaller than the average minority-carrier lifetime. Fossum and Shibib [12] divided the emitter into two regions. They treated the region near the base-emitter junction, where the doping concentration gradient is large and the doping level is low, as a buffer region and diffusion dominant current was assumed near the surface where, in their model, the effective doping concentration is nearly constant. A special function dependence of minority carrier lifetime was assumed by Selvakumar [13] and the transport equations were solved analytically. Recently, del Alamo and Swanson [14] formalized the transport problem in an elegant way and developed a procedure for writing a fast converging computer program. They also developed a quasi-transparent emitter model which is valuable for thin emitter devices. This model calculates the excess minority-carrier density in the emitter, assuming no recombination in the volume, as an approximation; then, the volume losses are obtained using this unpertubed distribution.

The analytical models [8]-[14] are based on some specific assumptions about the transport mechanism or the geometry of the device. In contrast, de Castro and Rudan [15] recast the problem as an integral equation which was solved by using an iterative technique and

convergence of the solution was determined by examing the kernal.

In this paper we present a general closed-form analytical solution of the minority-carrier transport equations in the nonuniformly heavily doped emitter. The solution is in the form of a multiple integral series and can be applied for any doping profile and for any value of S. The doping (or position) dependence of all parameters is included in the solution. The general analytical solution can be simplified by truncating the solution at a finite order. We discuss in detail the three lowest order approximations: the zeroth-order quasi-neutral quasi-equilibrium approximation (QNQE), and the first-order and second-order approximations.

By combining the truncated approximations with the results of exact numerical simulations, we find that the simplified zeroth-order QNQE model, which includes only the first term of the integral series, is very accurate for partially transparent emitters in devices with low S. It thus applies to most bipolar transistors with polysilicon emitter contacts and to surface-passivated solar cells.

The first-order approximation contains the first two terms of the integral series and is basically identical to the analytical model of del Alamo and Swanson [14], but it is rigorously derived here. The first-order approximation is found to be inaccurate in emitters with high S (ohmic metal contact) and in deep non-transparent emitters. The second-order approximation, composed of the first three terms of the integral series, is accurate for both shallow and deep emitters for surfaces with both high and low S. The analytical models developed here have advantages relative to exact computer simulation. These advantages become emphasized in circuit or system design. Exact computer

simulation rules out considering more than one physical make-up of a device at a time. When analytical models are available, many different physical make-ups are simultaneously considered in configuring a circuit to perform a given function. Thus, though at first sight it may seem contradictory, the availability of accurate analytical solutions of device behavior helps promote the possibility of design entirely by computer. In such a design, temperature, chemical species, and processing routines are entered, and circuit configurations yielding the desired electrical characteristics are obtained.

We note that the solution derived here, in the form of the multiple integral series, allows a compromise between simplicity and and accuracy to be attained by the choice of the number of terms employed. In addition, the different orders of approximation available provide perspective concerning solutions previously determined by more intuitive means.

The analytical solutions for the excess minority-carrier density in the emitter developed in this work also allow for the calculation of the quasi-static emitter charge and capacitance, and the transit time. These parameters are important for modeling of the transient and small-signal responses in bipolar transistors. In appendix B we derive the expressions for the above parameters in the zeroth-order approximation.

2.2 Theory

2.2.1 Transport Equations in Quasi-Neutral Emitter Region (QNE)

Consider a p-n junction by diffusing a n-type impurities into a uniform p-type substrate, as illustrated in Fig. 2.1. The steady-state

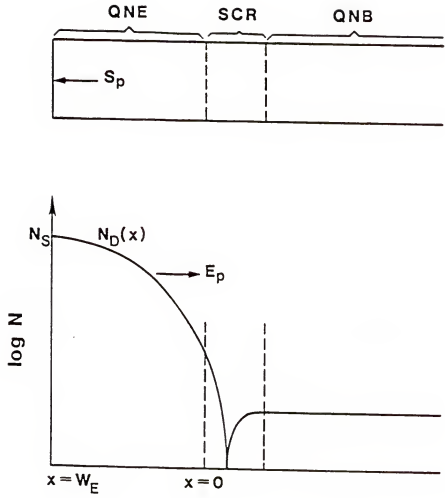

Figure 2.1 A one dimensional schematic diagram of the quasi-neutral emitter region and a graded doping profile used as an example.

transport equations in the QNE for the minority carriers injected from the base region are

$$J_n = q\mu_n n E_n + qD_n \frac{dn}{dx} \tag{2.1}$$

$$J_p = q\mu_p p E_p - qD_p \frac{dp}{dx} \tag{2.2}$$

$$\frac{dJ_p}{dx} = -q \frac{(p - p_0)}{\tau_p} \tag{2.3}$$

where p_0 is the equilibrium hole concentration. The rest of the parameters in (2.1)-(2.3) have their usual meaning. If we assume full ionization of the donor impurities atoms and low injection, $n(x)=N_D(x)$. The quasi-electric fields for electrons and holes [16], E_n and E_p, are equal to their equilibrium values E_{n0} and E_{p0}, respectively, in low injection. In equilibrium, the minority-hole concentration $p_0(x)$ is

$$p_0(x) = n_{i0}^2/N_{Deff} \tag{2.4}$$

where n_{i0} is the position independent intrinsic carrier concentration and N_{Deff} is the effective doping concentration defined as [17]

$$N_{Deff} = N_D \exp(-\Delta E_G/kT) \frac{\exp(E_F - E_C/kT)}{F_{1/2}(E_F - E_C/kT)} \tag{2.5}$$

in which $F_{1/2}$ is the Fermi integral of order half. The hole quasi-field can be then expressed as

$$E_p = -\frac{kT}{q} \frac{d}{dx} \ln(N_{Deff}) \quad . \tag{2.6}$$

Substituting (2.6) into (2.3) yields

$$J_p = -qD_p\, p \frac{d}{dx} \ln (N_{Deff}) + \frac{dp}{dx} \quad . \tag{2.7}$$

The first term on the right side of (2.7) is the drift current and the second term is the diffusion current. Equation (2.7) coupled with (2.3) forms a homogenuous second-order differential equation. Boundary conditions at x=0 and x=W_E are

$$p(0) = \frac{{n_{i0}}^2}{N_{Deff}(0)} \exp (qV_{BE}/kT) - 1 \tag{2.8}$$

$$J_p(W_E) = qS_p\, [p(W_E) - P_0(W_E)] \approx qS_p p(W_E) \tag{2.9}$$

where S_p is the surface recombination velocity for holes at the emitter contact and V_{BE} is the base-emitter junction voltage.

2.2.2 Integral Representation of the Analytical Solution

Integration of (2.7) from zero to x gives

$$p'(x) = p_0(x) \left[1 - \frac{1}{q} \int_0^x dx' \frac{1}{D_p(x')\, p_0(x')} J'(x') \right] , \tag{2.10}$$

where p'(x) and J'(x) are the normalized excess hole concentration and current

$$p'(x) = \frac{[p(x) - p_0(x)]}{\exp(qV_{BE}/kT) - 1} \tag{2.11a}$$

$$J'(x) = \frac{J_p(x)}{\exp(qV_{BE}/kT) - 1} \quad . \tag{2.11b}$$

The second term in (2.10) causes p'(x) to differ from the local equilibrium value $p_0(x)$. Integrating (2.3) yields J'(x) as a function of x

$$J'(x) = J'(0) - q \int_0^x \frac{p'(x')}{\tau_p(x)} \, dx' \quad . \tag{2.12}$$

Substituting J'(x) in (2.12) to (2.10) yields

$$p'(x) = p_0(x) \left[1 - \frac{1}{q} \int_0^x \frac{dx'}{D_p(x') \, p_0(x')} \right.$$
$$\left. \left(J'(0) - q \int_0^{x'} dx'' \frac{p'(x'')}{\tau_p(x'')} \right) \right] \quad . \tag{2.13}$$

Iterative analytical expressions for p'(x) can be obtained by substituting p'(x) from (2.10) into the right side of (2.13) and then by repeatedly following the same procedure used to derive (2.13) from (2.10) and (2.12)

$$p'(x) = p_0(x) \left[1 - \frac{J'(0)}{q} \sum_{i=1}^{\infty} A_{2i-1}(x) + \sum_{i=1}^{\infty} B_{2i}(x) \right] \tag{2.14}$$

where

$$A_{2i-1}(x) = \int_0^x dx_1 \frac{1}{D_p(x_1) \, p_0(x_1)} \int_0^{x_1} dx_2 \frac{p_0(x_2)}{\tau_p(x_2)}$$
$$\cdots \int_0^{x_{2i-2}} \frac{dx_{2i-1}}{D_p(x_{2i-1}) \, p_0(x_{2i-1})} \tag{2.15}$$

and

$$B_{2i}(x) = \int_0^x dx_1 \frac{1}{p(x_1)\, p_0(x_1)} \int_0^{x_1} dx_2 \frac{p_0(x_2)}{\tau_p(x_2)} \cdots \int_0^{x_{2i-1}} dx_{2i} \frac{p_0(x_{2i})}{\tau_p(x_{2i})} \quad . \tag{2.16}$$

From (2.10) and (2.13) we can see that the convergency of the excess hole density p'(x) expressed in (2.14) towards the actual accurate value is assured because

$$\frac{1}{q} \int_0^{W_E} dx\ J_p(x)/[D_p(x)p_0(x)] \quad < 1$$

and

$$\left[\frac{1}{q} \int_0^{W_E} dx\ p'(x)/\tau_p(x)\right] / J'(0) \quad < 1 \quad .$$

Applying the boundary condition (2.9) at $x=W_E$ gives the surface recombination current

$$J'(W_E) = qS_p p_0(W_E) \left[1 - \frac{J'(0)}{q} \sum_{i=1}^{\infty} A_{2i-1}(W_E) + \sum_{i=1}^{\infty} B_{2i}(W_E)\right] . \tag{2.17}$$

The bulk or volume recombination current can be written as

$$J'_{bulk} = q \int_0^{W_E} dx \frac{p_0(x)}{\tau_p(x)} \left[1 - \frac{J'(0)}{q} \sum_{i=1}^{\infty} A_{2i-1}(x) + \sum_{i=1}^{\infty} B_{2i}(x)\right] . \tag{2.18}$$

Thus from (2.17) and (2.18), the emitter saturation current is

$$J_0 = J'(0) = J'(W_E) + J'_{bulk}$$

$$= q \frac{\int_0^{W_E} dx \left[\frac{p_0(x)}{\tau_p(x)}\right] \left[1 + \sum_i B_{2i}(x)\right] + S_p p_0(W_E) \left[1 + \sum_i B_{2i}(W_E)\right]}{1 + \int_0^{W_E} dx \left[\frac{p_0(x)}{\tau_p(x)}\right] \sum_i A_{2i-1}(x) + S_p p(W_E) \sum_i A_{2i-1}(W_E)} . \tag{2.19}$$

For uniform doping concentration, (2.19) simplifies to

$$J_0 = qp_0 \frac{\frac{L_p}{\tau_p}\left[\sum_{i=0}^{\infty} \frac{1}{(2i+1)!}\left(\frac{W_E}{L_p}\right)^{2i+1}\right] + S_p \sum_{i=0}^{\infty} \frac{1}{(21+1)!}\left(\frac{W_E}{L_p}\right)^{2i}}{\sum_{i=0}^{\infty} \frac{1}{2i}\left(\frac{W_E}{L_p}\right)^{2i} + (S_p L_p/D_p) \sum_{i=0}^{\infty} \frac{1}{(2i+1)!}\left(\frac{W_E}{L_p}\right)^{2i+1}} \tag{2.20}$$

Equation (2.20) is the series-expansion expression for the saturation current for the uniformly doped case for which the exact solution is

$$J_0 = qp_0 \frac{(L_p/\tau_p) \sinh (W_E/L_p) + S_p \cosh (W_E/L_p)}{\cosh (W_E/L_p) + (S_p L_p/D_p) \sinh (W_E/L_p)} . \tag{2.21}$$

Thus, (2.20) serves as a check that the general solution (2.19) is correct.

The normalized local hole distribution (2.14) is a pertubation expansion around the local equilibrium concentration. Fast convergence of this series requires that the second term in (2.10) be much smaller than unity.

$$\frac{1}{q} \int_0^x dx' \frac{J'(x')}{D_p(x')\, p_0(x')} \ll 1 . \tag{2.22}$$

We can reformulate this condition in terms of a reduced hole quasi-Fermi potential $\phi_p'(x)$, defined as

$$p'(x) = p_0(x) \exp [q\phi_p'(x)/kT] \tag{2.23}$$

$$J'(x) = - qp'(x) \mu_p \frac{d\phi_p'}{dx} \tag{2.24}$$

where $\phi'_p = \phi_p - V_{BE}$. Introducing (2.24) into (2.22), we obtain

$$\exp [q\phi_p'(0)/kT] - \exp [q\phi_p'(x)/kT] \ll 1 \quad . \tag{2.25}$$

Hence fast convergence is obtained if $\phi'_p(x)$ is nearly spacially independent in the QNE. This quasi-equilibrium (QE) condition is satisfied in the space-charge region of the p-n junction where the large diffusion and drift components nearly balance each other even under forward bias, and both electron and hole quasi-Fermi levels are flat.

As will be shown later, this extended QE condition is satisfied also in the QNE with small S_p and $W_E \ll L_p$. For emitters with large S_p and or for emitters with $W_E \gg L_p$, deviations from this condition increase with distance from x=0. However, for most practical applications, the first three terms of (2.19) give sufficient accuracy, as will be shown later.

2.2.3 Approximation of the Solution by Truncating at Finite Order

A) Zeroth-Order Approximation:

Truncating the general expression (2.19), we can approximate the solution. The simplest approximation is to take only the first term in

(2.14)

$$p'(x) \approx p_0(x)$$

or

$$p(x) \approx p(x)[\exp(qV_{EB}/kT) - 1] \quad . \tag{2.26}$$

In other words, approximation (2.26) states that the normalized minority-hole concentration equals the equilibrium concentration. Referral to the usual energy-band diagram will show that this is equivalent to the condition that the minority-carrier quasi-Fermi level is independent of position x in the quasi-neutral emitter and reminds one of the conditions prevalent in equilibrium. Thus we call this the quasi-neutral quasi-equilibrium approximation (QNQE), the prefix QN being attached to distinguish from the QE approximation often made in a p-n junction space-charge region under forward voltage.

Boundary condition at $x=W_E$ gives the surface recombination current

$$J'(W_E) = qS_p(W_E) \quad . \tag{2.27}$$

The bulk recombination current is

$$J'_{bulk} = q\int_0^{W_E} dx \; \frac{p_o(x)}{J_p(x)} \quad . \tag{2.28}$$

Therefore,

$$J_0 = qn_{i0}^2 \int_0^{W_E} dx \; \frac{1}{\tau_p(x)\; N_{Deff}(x)} + \frac{S_p}{N_{Deff}(W_E)}$$

$$= qn_{i0}^2 \int_0^{W_E} dx \frac{1}{L_p^2(x)} \frac{D_p(x)}{N_{Deff}(x)} + \frac{S_p}{N_{Deff}(W_E)} \quad . \tag{2.29}$$

Intuitively, we can understand the formation of the QNQE condition when the surface recombination velocity is small and the emitter is thin, regardless of the direction of the built-in electric field due to the position dependent doping profile and the consequent $N_{Deff}(x)$. Consider first a retarding electric field. Suppose the diode is abruptly switched from reverse to forward voltage. This injects minority carriers into the edge of the quasi-neutral region of the base-emitter junction. A large diffusion current starts to flow. Since few of the injected carriers recombine because the emitter is thin and S_p is small, the minority carriers will start to accumulate inside the emitter region. Thus, as time passes, the minority-hole drift current will increase and the minority-hole diffusion current will decrease. The resulting trend is torward balance (quasi-equilibrium). Therefore, the adequency of the QE approximation depends on the thickness of the emitter region, on S_p and on the drift field directed away from the surface (retarding field).

When the built-in field is directed away from the edge of the emitter space-charge region, where the carriers are injected, considerations of the events following switching will show that direction of the diffusion current in the steady state will again oppose and will tend to balance the drift current and the total number of excess holes in the emitter is larger than that for a retarding field. This increases the bulk recombination current. Therefore, the emitter thickness should be smaller for this enhancement built-in field

case in order to have the same accuracy of the truncated solution as for the retarding field case. The trend toward near balancing of the drift and diffusion components (quasi-equilibrium of minority holes in the quasi-neutral emitter) becomes plain also for the extreme case of vanishing small surface recombination velocity. At the surface the minority-hole current must vanish; thus its drift and diffusion components must be equal in magnitude and oppositely directed.

As will be shown in Section 2.3, the transport in modern bipolar transistors with a polysilicon emitter contact and also in passivated solar cells is very well described by the zeroth-order QNQE approximation.

B) First-Order Approximation:

If we include A_1 in (2.14) and (2.19), then $p'(x)$ and J_0 can be approximated by

$$p'(x) = p_0(x) \left[1 - \frac{J_0}{q} A_1(x)\right] \tag{2.30}$$

$$J_0 = q \frac{\int_0^{W_E} dx \frac{p_0(x)}{\tau_p(x)} + S_p p_0(W_E)}{1 + \int_0^{W_E} dx \frac{p_o(x)}{\tau_p(x)} A_1(x) + S_p p_0(W_E) A_1(W_E)} . \tag{2.31}$$

The main feature of the first-order approximation is the assumption of a spatially independent current in calculating the excess concentration in (2.10), while in the zeroth-order approximation the current was assumed to be zero. For $\tau_p \to 0$, (2.31) reduces to the transparent emitter approximation of Shibib et al. [11].

An expression similiar to (2.31) was obtained by del Alamo and

Swanson [14] as a pertubation to the transparent emitter case. We can show here that, using the assumption of position independent J_p , the model of [14] can be derived by integrating (2.7) from x to W_E and approximating the constant current as $J_p(W_E)$:

$$p'(x) = p_0(x) \frac{J'(W_E)}{q} \left[\frac{1}{S_p p_0(W_E)} + \int_x^{W_E} dx' \frac{1}{D_p(x') p_0(x')} \right] \qquad (2.32)$$

$$J_0 = q n_{i0}^2 \left(\frac{NUM}{DEN} \right)$$

$$NUM = \int_0^{W_E} dx \frac{1}{L_p^2(x)} \frac{D_p(x)}{N_{Deff}(x)} + \frac{S_p}{N_{Deff}(W_E)} \left[1 + \int_0^{W_E} dx \frac{1}{L_p^2(x)} \cdot \frac{D_p(x)}{N_{Deff}(x)} \int_x^{W_E} dx' \frac{N_{Deff}(x')}{D_p(x')} \right]$$

$$DEN = 1 + [S_p / N_{Deff}(W_E)] \int_0^{W_E} dx \, [N_{Deff}(x)/D_p(x)] \qquad (2.33)$$

The expression (2.33) is identical to the expression (2.40) given in [14].

In (2.30), the local excess hole concentration is overestimated while it is underestimated in (2.32). When S_p is small bulk recombination dominates J_0 and its magnitude lies between the two values obtained from (2.31) and (2.33). The zeroth-order QNQE approximation assumes a constant current $J_p = 0$, so it is a part of a first-order approximation. In the limit of low S_p, there is no difference between the two approximations if the denominator of (2.31) is nearly equal to one. The second term in the denominator of (2.31) gives a wrong correction to the second order in W_E/L_p, which, however,

will negligibly affect the accuracy. The third term in the denominator of (2.31) is smaller than unity if

$$S_p \frac{1}{N_{Deff}(W_E)} \int_0^{W_E} dx \frac{N_{Deff}(x)}{D_p(x)} < S_p \int_0^{W_E} \frac{dx}{D_p(x)}$$

$$< S_p \int^{W_E} \frac{dx}{D_p(x)} \approx S_p \frac{W_E}{D_p} << 1 \quad , \tag{2.34}$$

where D_p is the average value in the emitter region

$$\frac{1}{D_p} = \frac{1}{W_E} \int_0^{W_E} \frac{dx}{D_p(x)} \quad . \tag{2.35}$$

In devices with thin emitters $D_p/W_E \approx 10^4$ cm/s - 10^5 cm/s. Thus no advantage results from using the more complicated first-order approximation instead of using zeroth-order QNQE approximation for values of S_p for which $S_p/(D_p/W_E) \ll 1$. For $S_p > W_E/D_p$, the correction by the third term in the denominator of (2.31) is significant, and cannot be neglected. The first-order approximation is consequently more accurate for large values of S_p than the zeroth-order QNQE approximation.

C) Second-Order Approximation:

If we keep A_1 and B_2 in (2.14) and (2.19), then we obtain the second order approximation for p' and J_0

$$p'(x) = p_0(x) \left[1 - \frac{J'(0)}{q} A_1(x) + B_2(x)\right] \tag{2.36}$$

$$J_0 = q \frac{\int_0^{W_E} dx \frac{p_0(x)}{\tau_p(x)} (1 + B_2(x)) + S_p p_0(W_E) (1 + B_2(W_E))}{1 + \int_0^{W_E} dx \frac{p_0(x)}{\tau_p(x)} A_1(x) + S_p p_0(W_E) A_1(W_E)} \quad . \tag{2.37}$$

The interpretation of these expressions become easier when we write down the second-order differential equation for $p'(x)/p_0(x)$. Defining

$$p'(x) = p_0(x) (1 - \alpha(x)) \tag{2.38}$$

and using (2.4) and (2.10), we obtain the second order differential equation for α

$$\frac{d^2\alpha(x)}{dx^2} + \frac{d}{dx} \left[\ln \left(\frac{D_p}{N_{Deff}} \right) \right] \frac{d\alpha(x)}{dx} = \frac{\alpha(x) - 1}{L_p^2} \quad . \tag{2.39}$$

If we neglect the correction term $\alpha(x)$ in the right side of (2.39), then (2.39) becomes a first-order differential equation for $d\alpha(x)/dx$ that can be solved analytically. The results are (2.36) and (2.37). On the other hand, the first order approximation neglects the bulk recombination in obtaining the position dependence of the excess hole concentration; thus it neglects the right side of (2.39) completely.

For uniform doping, (2.36) and (2.37) are accurate to the second order in W_E/L_p for low S_p. For fixed W_E, the accuracy decreases for higher S_p because the QE condition becomes valid and the order of accuracy becomes slightly worse than $(W_E/L_p)^2$.

2.3 Comparison of the Truncated Solutions with Computer Results

To compare the analytic truncated solutions of the series expansion, we wrote a computer program that numerically solves the minority-carrier transport equations in the quasi-neutral emitter region. The number of mesh points was between 100 and 400 depending on the required accuracy of 0.1 percent, i.e.,

$$0.999 < \left|[J'(W_E) - J'(0)]\right|/q \int_0^{W_E} [p'(x)/r(x)]\, dx \Big| < 1.001 \ .$$

To compare the analytical model with the computer simulations we use, as an example, the data of Slotboom and de Graaf [18] for bandgap narrowing and the expressions given by Arora et al. [19] for the hole diffusion coefficient.

$$\Delta E_G(N_D) = 9 \times 10^{-3} \left[\ln\left(10^{-17} N_D\right) + \left(\ln\left(10^{-17} N_D\right)\right)^2 + 1/2\right)^{1/2}\right] \quad [\text{eV}] \tag{2.40}$$

$$\mu_p(N_D) = \frac{54.3 \times (T/300)^{-0.57} \times 1.36 \times 10^8 \times T^{-2.23}}{1 + \dfrac{N_D}{2.35 \times 10^7 \times (T/300)^{2.4}} \times 0.88\,(T/300)^{-0.146}} \quad [\text{cm}^2/\text{Vs}] \tag{2.41}$$

The degeneracy of the majority carriers has been included with effective mass $m^*_n = 1.1\, m_0$ [20]. The Auger coefficient measured by Dziewior and Schmid [21] are chosen and Shockley-Read-Hall (SRH) recombination coefficient is from Lee [22]. Throughout our comparison, a Gaussian doping profile has been assumed with $N_D(W_E) = 10^{20}$ cm^{-3} and $N_D(0) = 10^{18}$ cm^{-3} (Fig. 2.1).

Fig. 2.2 shows the local near counter-balance of the minority hole drift and diffusion currents through the emitter region for $W_E = 0.2$ μm and $S_p = 10^3$ cm/s. The exact value of the saturation current is 2.073×10^{-13} A/cm^{-2} while the zeroth and first-order approximation results are 2.185×10^{-13} A/cm^{-2}, which is accurate to 5 percent. The second-order approximation gives 2.075×10^{-13} A/cm^2 which is accurate within 0.1 percent. We can see that the QNQE condition is not strictly satisfied near $x = W_E$ for large S_p (Fig. 2.3) or large W_E (Fig. 2.4).

Figure 2.5 displays the saturation current for different emitter thicknesses for $S_p = 10^7$ cm/s. When the emitter is thin and S_p is high, then the saturation current is nearly equal to the surface recombination current. The saturation currents for $S_p = 1000$ cm/s are shown in Fig. 2.6. Because the Auger recombination lifetime is shown, the emitter saturation current is nearly equal to the bulk recombination current. Therefore, the saturation current increases as W_E increases and converges to a value for the opaque emitter case.

Figure 2.7 shows the equai-percent-error lines for zero, first, and second-order approximations for the emitter saturation current. As anticipated from section 2.2, each approximation becomes more accurate as S_p gets smaller. Most modern silicon bipolar transistors and solar cells have $W_E < 0.3$ μm; the accuracy of the first-order approximation is within 15 percent. For $S_p \leq 5 \times 10^4$ cm/s, there is no difference in accuracy between the zeroth and first-order approximation. As we can see in Fig. 2.7, the improvement of the accuracy is outstanding when the second-order approximation is used.

Figures 2.2 - 2.7 show the comaprison of our analytical model with exact computer solutions for certain sets of parameters, chosen for

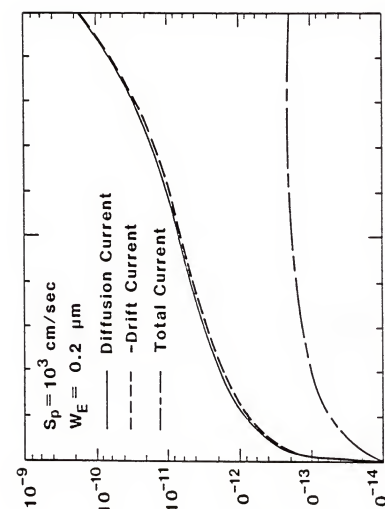

Figure 2.2 Near quasi-equilibrium condition in the emitter region (W_E = 0.2 um, $S_p = 10^3$ cm/s, $N_D(W_E) = 10^{20}$ cm^{-3}, $N_D(0) = 10^{18}$ cm^{-3}).

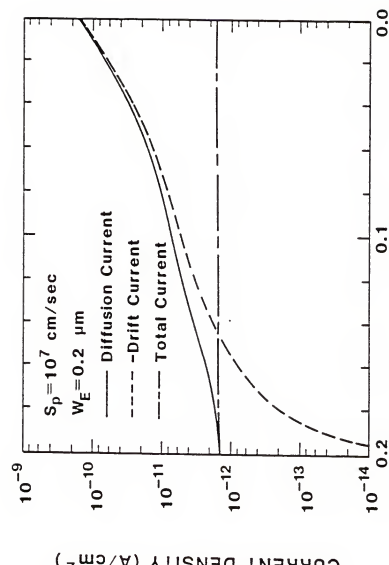

Figure 2.3 Breakdown of the quasi-equilibrium condition near the surface for high surface recombination velocity (W_E = 0.2 um, S_P = 10^7 cm/s, $N_D(W_E)$ = 10^{20} cm^{-3}, $N_D(0)$ = 10^{18} cm^{-3}.)

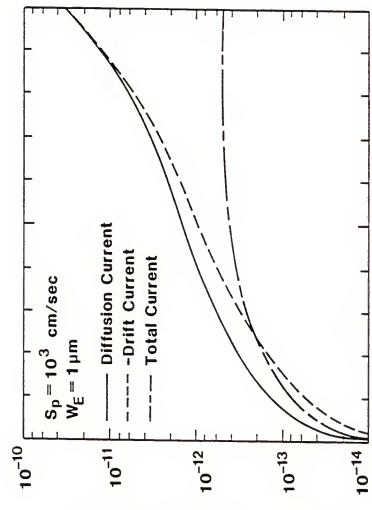

Figure 2.4 Breakdown of the quasi-equilibrium condition near the surface for opaque emitter (W_E = 1 um, Sp = 10^3 cm/s, $N_D(W_E) = 10^{20}$ cm^{-3}, $N_B(0) = 10^{18}$ cm^{-3}).

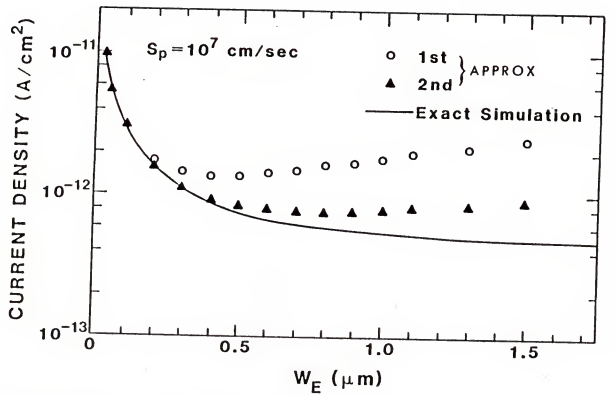

Figure 2.5 Comparison of numerical solution with the first- and second-order approximations for various emitter widths ($S_p = 10^7$ cm/s, $N_D(W_E) = 10^{20}$ cm^{-3}, $N_D(0) = 10^{18}$ cm^{-3}).

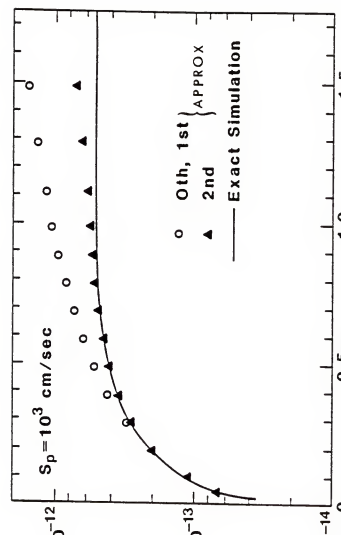

Figure 2.6 Comparison of numerical solution with truncated solutions ($S_p = 10^3$ cm/s, $N_D(W_E) = 10^{20}$ cm^{-3}, $N_D(0) = 10^{18}$ cm^{-3}).

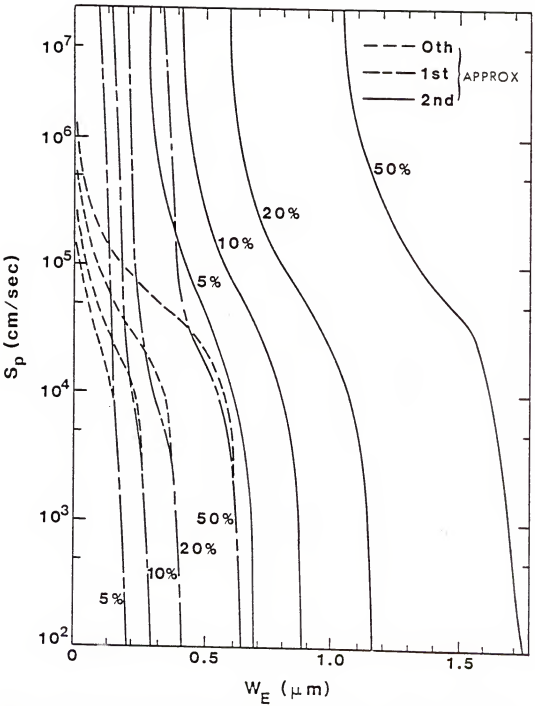

Figure 2.7 Equal-percent-error lines for zeroth-, first, and second order approximations for J_0.

demonstration purposes. Choice of other parameters showed similiar agreement. The accuracy of the model is not parameter dependent.

2.4 Conclusions

The transport of minority carriers injected into a heavily doped emitter region has been analyzed systematically. The infinite series of integral terms of our central result can be truncated depending on the accuracy needed. The three lowest order approximations are discussed in detail, related to the earlier results, and assessed by comparison with accurate numerical solutions (see Fig. 2.7). For many devices the simplest approximation given by (2.29) is sufficiently accurate and is much simpler than the previous solutions. This is termed the quasi-neutral quasi-equilibrium approximation, which is a physically revealing name. Though we have emphasized heavily doped silicon emitters, the method holds generally for quasi-neutral regions of semiconductors having position-dependent composition and parameters, as in heterojunction bipolar transistors.

Analytical solutions (2.14) and (2.19) show that the steady state current can be described if the bulk parameter D_p/N_{Deff} and L_p and the surface parameter $S_p/N_{Deff}(W_E)$ are known [23]. Del Alamo et al. [23] analyzed the existing data for bandgap narrowing, lifetime, and diffusion length, and concluded that there is a sufficient agreement in the measurement of D_p/N_{Deff} and L_p among various investigators, even though there is a wide scatter in D_p and N_{Deff} separately. Figures 2.5 - 2.7 are based on the values of N_{Deff} calculated from the Slotboom and de Graff model for bandgap narrowing ΔE_G [18]. In order to calculate these graphs for other models of ΔE_G, the value of S_p in Fig. 2.5 - 2.7

should be adjusted accordingly for the constant ratio of S_p/N_{Deff}.

Equation (2.14) is a general expression for the excess minority-carrier concentra tion in the emitter. Based on (2.14) we have derived expressions for the steady-state current in various levels of approximations. From (2.14) we can also calculate the other important charge-control relations for the total charge stored in the quasi-neutral emitter Q_E, the quasi-static capacitance C_E, and the emitter charge-control time constant τ_E. These relations are derived in the Appendix B for the zeroth-order approximation case. Similiar, but more complicated, expressions can be also derived for the higher order approximations.

CHAPTER THREE
DETERMINATION OF BANDGAP NARROWING FROM ACTIVATION PLOTS

3.1 Introductionn

Various experimental methods exist to determine bandgap contraction and minority-carrier mobility and diffusivity in heavily doped silicon, parameters that play a central role in characterizing p-n junction diodes, transistors, and solar cells. Some methods use the recombination current in the quasi-neutral emitter of a diode or transistor. These fall into two categories: a) those that assume equality between the majority-carrier mobility and minority-carrier mobility [18],[24]-[26]; and b) those that avoid this assumption, which has been questioned [27], [28], by emphasizing the temperature dependence of this recombination current [29]. The latter category has produced values of bandgap reduction considerably larger than the values derived from other methods [18],[24]-[26].

In the present study, we use method b), attempting to improve its accuracy by varying the minority-carrier surface recombination velocity at the emitter contacts of otherwise nearly identical emitters. This approach yields $\Delta E_G = 133 \pm 6$ meV ($m^*_n = 1.45\ m_0$) and $\Delta E_G = 149 \pm 6$ meV ($m^*_p = 1.1\ m_0$) for a Si:As emitter having an approximately space-independent doping concentration of 10^{20} cm^{-3}. Also it yields minority carrier diffusion length $L_p = 0.23$ μm. The value for ΔE_G obtained by

this method shows better agreement with other determinations than do those obtained previously by using the temperature dependence of emitter recombination currents [29].

3.2 A Simple Theory for the Interpretation of the Experimental Results

We consider a uniformly doped shallow quasi-neutral emitter region (QNE: $0 \leq x \leq W_E$) of a n-p-n bipolar transistor. The emitter saturation current J_{SE} can be expressed as

$$J_{SE} = qn_{io}^2 \frac{D_p}{N_{Deff}} \frac{1}{L_p} \frac{(S_p/D_p)L_p + \tanh (W_E/L_p)}{1 + (S_p/D)\, L_p \tanh (W_E/L_p)}, \tag{3.1}$$

where S_p is the surface recombination velocity at $x = W_E$, N_{Deff} is the effective doping concentration, and the other symbols have their usual meanings. For large S_p ($S_p > D_p/W_E$), (3.1) can be approximated as

$$J_{SE}(S_p \to \infty) = qn_{io}^2 \frac{D_p}{N_{Deff}} \frac{1}{L_p} \coth (W_E/L_p) \tag{3.2}$$

For small $S_p (S_p < W_E/\tau_p)$, (3.1) has the following asymptotic form:

$$J_{SE}(S_p \to 0) = qn_{io}^2 \frac{D_p}{N_{Deff}} \frac{1}{L_p} \tanh (W_E/L_p) \tag{3.3}$$

Usually efforts to separate N_{Deff} and D_p have involved measuring $J_{SE}(S_p \to \infty)$ for devices with shallow emitters and ohmic contacts at $x = W_E$. In the analysis of these measurements, assumptions about the minority-carrier diffusion coefficient D_p were used, although the validity of these values cannot be confirmed by direct measurement.

We can avoid these uncertainties by measuring J_{SE} for a device

with $S_p \to 0$ and $W_E < L_p$. In this limit (3.1) reduces to

$$J_{SE}(S_p \to 0) \approx q n_{i0}^2 \frac{D_p}{N_{Deff}} \frac{W_E}{\tau_p} . \tag{3.4}$$

By $S_p \to 0$, we mean that $S_p < W_E/\tau_p$. In (3.4), the neglect of the surface recombination velocity at $x = W_E$ means that J_{SE} is the recombination current within the volume or bulk of the quasi-neutral emitter. Dziewior and Schmid [21] measured τ_p from the photoluminescence decay emitted from the n-type bulk silicon after excitation by a laser pulse, and showed that τ_p is independent of temperature in the range $300\ K < T < 400\ K$. Therefore, the temperature dependence of $J_{SE}(S_p \to 0)$ is determined only by n_{i0}^2/N_{Deff} where

$$n_{i0}^2 = N_c N_v \exp(-E_{GI}/kT) \tag{3.5}$$

is the square of the standard intrinsic density, N_c and N_v are the electron and hole effective density of states, respectively, and E_{GI} is the intrinsic energy gap. The temperature dependence of E_{GI} is [30]

$$\begin{aligned} E_{GI} &= E_{GI}(0) - \alpha T \\ &= 1.206 - 2.8\ E\text{-}4\ T \quad (eV) . \end{aligned} \tag{3.6}$$

In (3.6) $E_{GI}(0)$ is the linearly extrapolated energy gap, which differs from the actual energy gap of 1.170 eV at 0 K. Assuming the rigid band approximation and including the Fermi-Dirac statistics, we can express N_{Deff} as

$$N_{Deff} = N_D \exp(-\Delta E_F/kT) \exp(\epsilon_c)/F_{1/2}(\epsilon_c) , \tag{3.7}$$

where ΔE_G is the reduced bandgap energy, $F_{1/2}$ is the Fermi-Dirac

integral of order half and $\epsilon_c = (E_F - E_C)/kT$. Substituting (3.5), (3.6), and (3.7) into (3.4), we get the following relation:

$$d \ln \left[J_{SE}(S_p \to 0)\, T^{-\alpha} \exp\left[\epsilon_c(T)\right]/F_{1/2}[\epsilon_c(T)] \right] d(kT)^{-1}$$

$$= -\left[E_{GI}(0) - \Delta E_G\right] + (kT)^{-1}\, d\Delta E_G/d(kT)^{-1} \quad (\alpha = 3.0) \tag{3.8}$$

Comparison of ΔE_G measured by photoluminescence at 10 K [31] and around room temperature [32] shows that the values of ΔE_G are temperature independent within the experimental accuracy of about ±10 meV. A similar temperature independence of ΔE_G was observed in optical absorption experiments [33]. Thus the second term in (3.8) can be neglected. Other details for extracting ΔE_G are explained in Neugroschel et al. [29].

3.3 Experimental Results and Discussions

For our experimental study, the emitter saturation currents of two n-p-n bipolar transistors were measured in the temperature range of $300K < T < 360$ K. The two transistors have nearly uniform emitter doping profile, $N_{DD} \approx 10^{20}$ cm^{-3} and $W_E = 0.18$ μm, but one (device A) has an ohmic contact at the surface and the other (device B) has an polysilicon emitter contact.

Although the mechanisms underlying the improved current gain and low surface recombination velocity in transistors with polysilicon contacts are still debated in the literature, there is sufficient evidence that the surface recombination velocity at the polysilicon-monosilicon interface can be much smaller than 10^4 cm/s [34]-[36]. A recent experimental study by Neugroschel et al. [34], using test

structures with polysilicon emitter contacts similar to the polysilicon contact of device B, estimated $S_p \approx 1000$ cm/s. As mentioned earlier, the assumption that $S_p \to 0$ requires that $S_p < W_E/\tau_p$, which is satisfied for the device B, as discussed above.

As a first step in our procedure, the minority-hole diffusion length L_p is determined from the ratio of J_{SE} for devices A and B, $J_{SE}(S_p \to \infty)/J_{SE}(S_p \to 0)$ at the same temperature. From (3.2) and (3.3)

$$L_p = W_E/\text{arccoth } [J_{SE}(S_p \to \infty)/J_{SE}(S_p \to 0)]^{1/2} . \qquad (3.9)$$

The measured ratio of $J_{SE}(S_p \to \infty)/J_{SE}(S_p \to 0)$ at 300 K was 2.4 and L_p deduces from (3.9) is about 0.23 μm. The ratio of $J_{SE}(S_p \to \infty)/J_{SE}(S_p \to 0)$ was also measured in the temperature range of 100 K - 400 K and ranged from 2.2 to 2.4. This indicates that L_p is a weak function of temperature between 100 - 400 K.

The bandgap shrinkage ΔE_G is obtained from the temperature dependence of device B using (3.4), in the temperature range from 300 - 360 K, which yields $\Delta E_G = 149 \pm 6$ meV for an electron effective mass $m^*_n = 1.1\ m_0$: $\Delta E_G = 133 \pm 6$ meV for $m^*_n = 1.45\ m_0$. The results for two values of m^*_n are given because of uncertainties about the actual value of m^*_n [29], [37].

The above value for ΔE_G was derived from the activation plot of (3.4), an expression that is valid for $S_p \ll W_E/\tau_p$ and $W_E/L_p \ll 1$. The measured value for L_p is about 0.23 μm, ie, $W_E/L_p \approx 0.78$. Thus we have to investigate the temperature dependence of (D_p/L_p) tanh (W_E/L_p) in (3.3). This requires an assumption about the temperature dependence of D_p. We assume, for the purpose of a sensitivity study only, that D_p is proportional to T. Under this assumption the error in $\Delta E_G = 149$ meV is

about 4 meV for $S_p \ll W_E/\tau_p$. The sensitivity to S_p can be established by assuming $S_p = 10^4$ cm/s (for $W_E/L_p \ll 1$) which causes an error of about 4 meV. The combined effects of finite S_p and $W_E/L_p \leq 1$ for device B were examined using (3.1) and found to cause an error of about 8 meV. The temperature dependence of m^*_n is very small in the temperature range used [37] and was neglected.

For the comparison of our values for ΔE_G with other experimental results, we calculated the "apparent bandgap narrowing" ΔE_G^{app} [23]. Assuming Maxwell-Boltzmann statistics, ΔE_G is defined as

$$N_{Deff} = N_D \exp(-\Delta E_G^{app}/kT) \tag{3.10}$$

Therefore, the relation between ΔE_G^{app} and ΔE_G is

$$\Delta E_G^{app} = \Delta E_G + kT \ln[F_{1/2}(\epsilon_c) \exp(-\epsilon_c)] \ . \tag{3.11}$$

This gives $\Delta E_G^{app} = 118 \pm 6$ meV when $m^*_n = 1.1\ m_0$ or 113 ± 6 when $m^*_n = 1.45\ m_0$ at 300 K which are in close agreement with the published values of ΔE_G^{app} shown in del Alamo et al. [23, Fig. 1].

3.4 Conclusions

Transport phenomena in the heavily doped silicon were studied by measuring the emitter saturation currents for the n-p-n transistors with two different types of emitter contacts: ohmic contacts and polysilicon contacts.

From the measurements we conclude that at $N_D = 10^{20}$ cm^{-3}, $L_p \approx 0.23$ μm, and $\Delta E_G = 149$ meV for $m^*_n = 1.1\ m_0$ or $\Delta E_G = 133$ meV for $m^*_n = 1.45\ m_0$. These results correct the previous determinations [29] that yielded higher values for ΔE_G. The device exhibited I_B proportional to

$\exp(qV_{BE}/kT)$ over several decades of current. Thus no corrections for space-charge-region current components were required, which was not the case in Neugroschel et al. [29].

A similar approach employing the temperature dependence of the emitter saturation current to obtain bandgap narrowing appeared recently in the conference literature [38] with a different discussion of the underlying assumptions than that given in the present study. In part, this conference paper differs from the work of present study because the authors used $\alpha = 3.5$ instead of $\alpha = 3.0$ in (3.8); we base our choice of α on the condition that the bulk recombination exceeds the surface recombination in the single crystal silicon ($S_p < W_E/\tau_p$).

The method used here can be used to explore bandgap narrowing for various doping concentrations.

CHAPTER FOUR
NUMERICAL ANALYSIS OF THE MINORITY-CARRIER TRANSPORT IN BIPOLAR DEVICES UNDER SMALL-SIGNAL EXCITATION

4.1 Introduction

Exact numerical analysis of the minority-carrier transport in bipolar devices, such as p-n junctions and transistors, is necessary for accurate analysis and modeling of device operation. Various analytical and numerical methods of steady-state device simulation exist today. The AC numerical solutions published previously [39], [40] are one-dimensional contact-to-contact solutions. Some other possible techniques for obtaining the small-signal AC numerical solutions were recently reviewed by Laux [41].

In this work we develop a simple numerical method for a regional analysis of quasi-neutral regions under AC excitation. This regional analysis assumes that the device can be divided into quasi-neutral and space-charge regions and that the solutions for each region can be superimposed. Such an analysis has advantages in that its simplicity affords a detailed physical insight and interpretation. The model presented here is based on the linearity of the small-signal transport equations and applies for quasi-neutral regions in low injection. The method is used for the calculation of the small-signal equivalent circuit parameters, such as conductances and capacitances, of the emitter and base regions of bipolar transistors. Combined with a

separate solution for the space-charge region, this gives a complete device characterization. The AC solutions are compared with the quasi-static approximation over a wide frequency range. The difference between the quasi-static and small-signal capacitances are discussed in detail. The analysis implies that the quasi-static and small-signal capacitances are nearly equal in regions where the quasi-equilibrium condition prevails (Chapter 2). Since the quasi-equilibrium condition is satisfied in the space-charge region (SCR) under forward bias, we conclude that the SCR capacitance under AC excitation can be accurately approximated by its readily available quasi-static value C_{SCR} [42]. The combination of the numerical solutions with that for SCR allows the determination of the total equivalent base-emitter capacitance of a bipolar transistor.

In Section 4.2 we describe the developed numerical method that solves the small-signal transport equations in the quasi-neutral region. In heavily doped emitter we consider heavy doping effects and the conditions at the emitter surface, e.g., metal or polysilicon. In the limit of low frequency the AC solution is similar to that of del Alamo and Swanson [14]. Numerical simulation results for diodes and bipolar transistors and their physical interpretation are discussed in Section 4.3.

4.2 Small-Signal Transport Equations and Numerical Method

4.2.1 Small-Signal Transport Equations

In this Section we define the transport equations, boundary conditions, and assumptions used in the numerical simulation. Consider an n-type quasi-neutral region, $0 \leq x \leq W$. Suppose that DC and small

sinusoidal voltages are applied

$$V = V_0 + v \exp(i\omega t) \quad , \tag{4.1}$$

where V_0 is the constant DC voltage and v is the amplitude of the sinusoidal voltage which is small compared to the thermal voltage $V_T = kT/e$, such that

$$\exp(v/V_T) \simeq 1 + v/V_T \quad . \tag{4.2}$$

The minority holes are injected at the edge of the space-charge region at x = 0. We also assume that the surface can be characterized by an effective surface recombination velocity S_p at x = W. The one-dimensional transport equations describing the behavior of the minority holes in the n-region are

$$J_p = qp\mu_p E_p - qD_p \frac{\partial p}{\partial x} \tag{4.3}$$

$$\frac{\partial p}{\partial t} = -\frac{1}{q}\frac{\partial J_p}{\partial x} - \frac{(p - p_o)}{\tau_p} \quad , \tag{4.4}$$

where p_o is the equilibrium hole concentration, and the other parameters have their usual meaning. In equilibrium, p_o for a nonuniformly doped region can be expressed as

$$p_o(x) = n_{io}^2/N_{Deff}(x) \quad , \tag{4.5}$$

where N_{Deff} is the effective doping concentration that includes the heavy doping effects [17]. In solving equations (4.3) and (4.4) the following assumptions are made:

(a) the quasi-neutral region is in low injection;

(b) the phase delay due to the transport throuth the base-emitter space-charge region is neglected;

(c) the displacement current in the quasi-neutral region is neglected;

(d) the minority-carrier lifetime and mobility in the quasi-neutral region are frequency independent.

Using the assumptions (a) and (b), the hole concentration at x = 0 can be written as

$$p(0) = P(0) + \tilde{p} \exp(i\omega t) \simeq \frac{n_{io}^2}{N_{Deff}(0)} \exp\left[V_0 + \left(\frac{v}{V_T}\right)\right] \exp(i\omega t)]$$

$$\simeq \frac{n_{io}^2}{N_{Deff}(0)} \exp\left(\frac{V_0}{V_T}\right) \left[1 + \left(\frac{v}{V_T}\right) \exp(i\omega t)\right] \quad , \tag{4.6}$$

where P(0) is the DC component of the hole concentration. Separating the time varying components from the DC components, we obtain the small-signal transport equations for the real and imaginary components of the hole current

$$j_R(x) = - F(x) \frac{du_R}{dx} \tag{4.7}$$

$$j_I(x) = - F(x) \frac{du_I}{dx} \tag{4.8}$$

$$\frac{dj_R(x)}{dx} = -G(x) (u_R - \omega r_p u_I) \tag{4.9}$$

$$\frac{dj_I(x)}{dx} = -G(x) (u_I + \omega r_p u_R) \quad , \tag{4.10}$$

where

$$\tilde{p}(x) = \tilde{p}_R(x) + i\tilde{p}_I(x) \tag{4.11}$$

$$j(x) = j_R(x) + ij_I(x) \tag{4.12}$$

$$u(x) = u_R(x) + iu_I(x) = [p(x)N_{Deff}(x)]/n_{io}^2 \tag{4.13}$$

$$F(x) = qn_{io}^2 D_p(x)/N_{Deff}(x) \tag{4.14}$$

$$G(x) = qn_{io}^2/[\tau_p(x)N_{Deff}(x)] \quad . \tag{4.15}$$

Equations (4.7) - (4.10) are homogeneous linear differential equations for $j(x)$ and $\tilde{p}(x)$. For $\omega\tau_p \ll 1$, the coupling between the real and imaginary parts is small in equations (4.7) - (4.10). Coupling begins to be important for $\omega\tau_p \geq 1$.

The boundary conditions for $u(x)$ at $x = 0$ can be written as

$$u_R(0) = \exp(V_0/V_T)\ v/V_T = [\tilde{p}(0)\ N_{Deff}(0)]/n_{io}^2 \tag{4.16}$$

$$u_I(0) = 0 \quad . \tag{4.17}$$

The boundary conditions at the surface at x=W are

$$j_R(W) = \frac{qn_{io}^2}{N_{Deff}(W)}\ S_p u_R(W) \tag{4.18}$$

$$j_I(W) = \frac{qn_{io}^2}{N_{Deff}(W)}\ S_p U_I(W) \quad . \tag{4.19}$$

4.2.2 Numerical Method

In this section we describe the numerical method used to solve the small signal transport equations (4.7) - (4.10) with the boundary conditions (4.16) - (4.19).

As discussed earlier, (4.7) - (4.10) are a system of ordinary linear differential equations. The general solution is a linear combination of the four linearly independent solutions (modes). Suppose that we obtain a numerical solution for the first mode with arbitrary initial conditions at x=0, $u_R(0) = u_{R1}(0)$, $u_I(0) = u_{I1}(0)$, $j_R(0) = j_{R1}(0)$, and $j_I(0) = j_{I1}(0)$. In the same way, solutions for the three other modes with other arbitrary initial conditions at x = 0 can be obtained. The general solution is a linear combination of four modes

$$u_R(x) = \sum_{i=1}^{4} C_i u_{Ri}(x) \tag{4.20}$$

$$u_I(x) = \sum_{i=1}^{4} C_i u_{Ii}(x) \tag{4.21}$$

$$j_R(x) = \sum_{i=1}^{4} C_i j_{Ri}(x) \tag{4.22}$$

$$j_I(x) = \sum_{i=1}^{4} C_i j_{Ii}(x) \quad . \tag{4.23}$$

The coefficients C_i in (4.20) - (4.23) can be found by applying the boundary conditions (4.16) - (4.19)

$$\exp (V_0/V_T)\ v/V_T = \sum_i C_i u_{Ri}(0) \tag{4.24}$$

$$0 = \sum_i C_i u_{Ii}(0) \tag{4.25}$$

$$0 = \sum_i C_i \left[j_{Ri}(W) - \frac{q n_{i0}^2 S_p}{N_{Deff}(W)}\, u_{Ri}(W) \right] \tag{4.26}$$

$$0 = \sum_i C_i \left[j_{Ii}(W) - \frac{q n_{i0}^2 S_p}{N_{Deff}(W)}\, u_{Ii}(W) \right] \quad . \tag{4.27}$$

In addition to the AC solutions, the steady-state current and excess carrier distributions can be obtained in the limit of $\omega \to 0$.

4.3 Numerical Results and Discussion

The numerical method described in Section 4.2 was applied for the simulation of small-signal parameters of an n-p-n transistor using HP 9845 desktop computer. Figure 4.1 shows the doping profiles of an n-p-n bipolar transistor used for the simulation. The small-signal base current in the forward active mode neglecting the recombination current in the space-charge region can be written as

$$i_B = i_B^{(E)} + i_B^{(JE)} + i_B^{(B)} \quad . \tag{4.28}$$

In (4.28), $i_B^{(E)}$ is the recombination current of minority holes injected into the quasi-neutral emitter region, $i_B^{(JE)}$ is the emitter-base space-charge region charging current, and $i_B^{(B)}$ is the recombination current in the base region.

At first, we consider $i_B^{(E)}$ which is the main contribution to the base current in the forward active mode

$$j_B^{(E)} = i_B^{(E)}/A_E = [G^{(E)}(\omega) + i\omega C^{(E)}(\omega)]v_{be} \quad , \tag{4.29}$$

where A_E is the emitter area, and $G^{(E)}$ and $C^{(E)}$ are the small-signal conductance and capacitance. Figure 4.2 shows the numerical simulation results of $G^{(E)}$ and $C^{(E)}$ as a function of frequency in a normalized scale for the emitter doping profile shown in Fig. 4.1. The emitter doping profile is Gaussian changing from 10^{20} cm^{-3} at the surface to 10^{18} cm^{-3} at the edge of the emitter-base SCR. At low frequencies, $G^{(E)}$

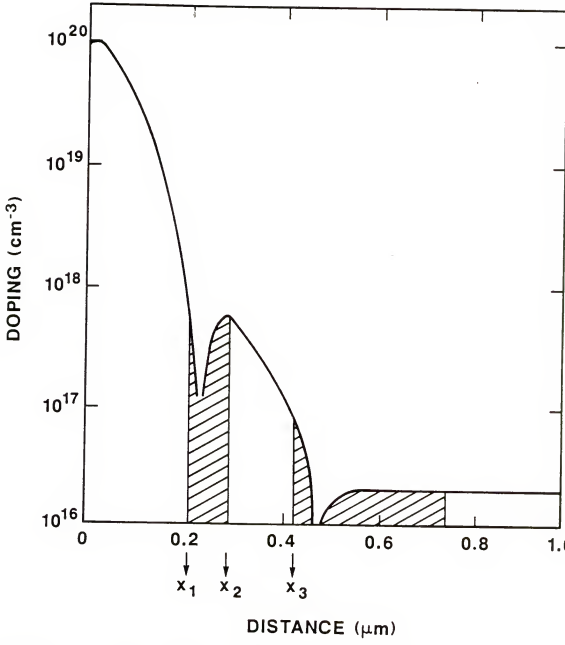

Figure 4.1 Doping profiles for n-p-n bipolar transistor used for the simulation. The positions of edges of the space-charge regions are given by x_1, x_2, and x_3. The quasi-neutral base width is 1400 Å, and the quasi-neutral base width is 2000 Å.

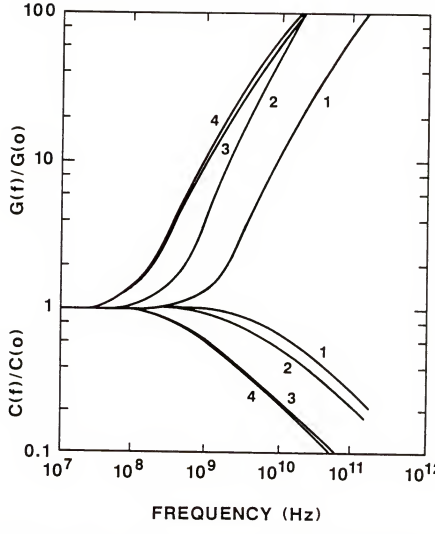

Figure 4.2 The dependence of the real and imaginary parts of the emitter admittance on frequency. Doping profile is Gaussian changing from 10^{20} cm^{-3} to 10^{18} cm^{-3}. (1)W_E = 0.2μm, S_p = 10^7cm/s, (2) W_E = 0.2 μm, S_p = 10^3 cm/s, (3) W_E = 1.0 μm, S_p = 10^7cm/s, (4) W_E = 1.0 μm, S_p = 10^3 cm/s.

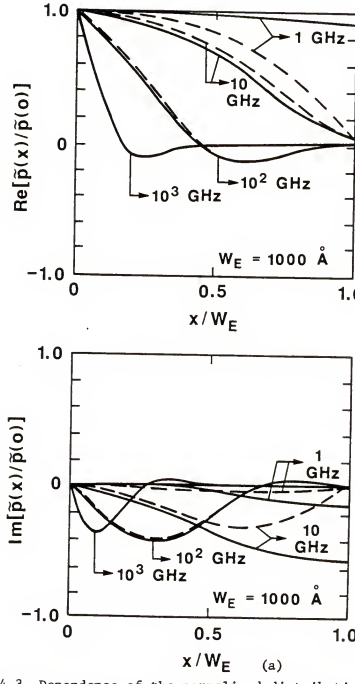

Figure 4.3 Dependence of the normalized distribution of the real and imaginary parts of the hole density in the emitter region on frequency. Emitter profile is Gaussian changing from 10^{20} cm^{-3} to 10^{18} cm^{-3}. Solid lines are for $S_p = 10^3$ cm/s and broken lines are for $S_p = 10^7$ cm/s. (a) $\mu_p = \mu_p(min)$, $W_E = 1000$ Å, (b) $\mu_p = \mu_p(min)$, $W_E = 2000$ Å, (c) $\mu_p = \mu_p(maj)$, $W_E = 1000$ A, (d) $\mu_p = \mu_p(maj)$, $W_E = 2000$ A.

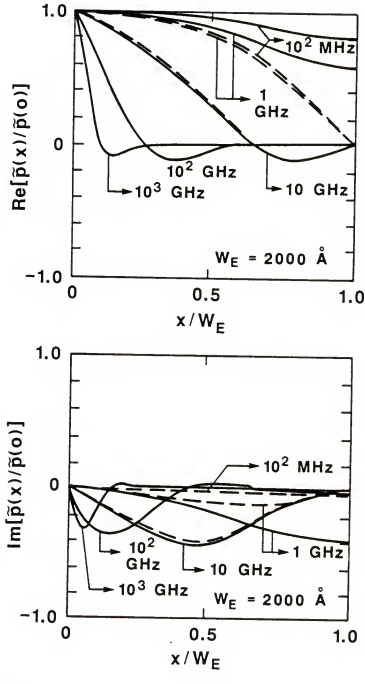
1.0
0
-1.0
Re[p̃(x)/p̃(o)]
10^2 MHz
1 GHz
10^2 GHz
10^3 GHz
10 GHz
W_E = 2000 Å
0
0.5
1.0
x/W_E
1.0
0
-1.0
Im[p̃(x)/p̃(o)]
10^2 MHz
10^2 GHz
1 GHz
10 GHz
10^3 GHz
W_E = 2000 Å
0
0.5
1.0
x/W_E

Figure 4.3 (b)

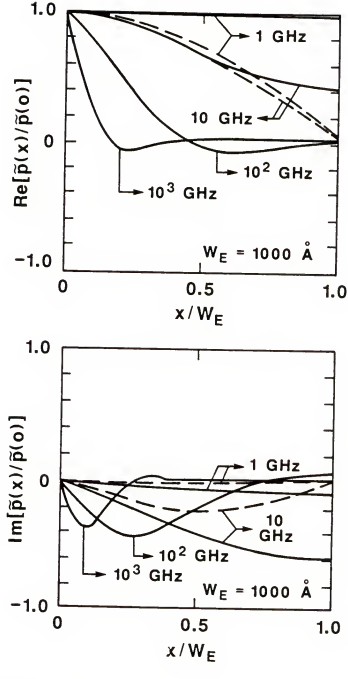
1.0
0
-1.0
Re[p̃(x)/p̃(o)]
1 GHz
10 GHz
10^2 GHz
10^3 GHz
W_E = 1000 Å
0
0.5
1.0
x/W_E
1.0
0
-1.0
Im[p̃(x)/p̃(o)]
1 GHz
10 GHz
10^2 GHz
10^3 GHz
W_E = 1000 Å
0
0.5
1.0
x/W_E

Figure 4.3 (c)

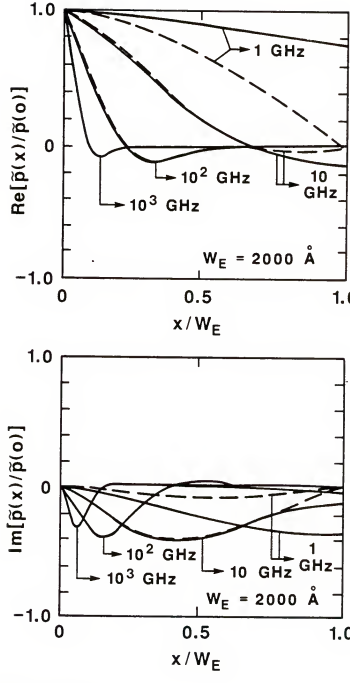
1.0
0
-1.0
Re[p̃(x)/p̃(o)]
1 GHz
10² GHz
10 GHz
10³ GHz
W_E = 2000 Å
0
0.5
1.0
x/W_E
1.0
0
-1.0
Im[p̃(x)/p̃(o)]
10² GHz
1 GHz
10 GHz
10³ GHz
W_E = 2000 Å
0
0.5
1.0
x/W_E

Figure 4.3 (d)

and $C^{(E)}$ are frequency independent and approach $G(E) \propto \omega^{1/2}$ and $C^{(E)} \propto \omega^{-1/2}$ in the high frequency limit.

Figs. 4.3 (a) - (d) display the real and imaginary parts of the hole distribution $\tilde{p}_R(x)$ and $\tilde{p}_I(x)$ in the emitter for different neutral emitter widths and surface recombination velocities. In the numerical simulations, we have assumed that Auger recombination lifetime from Dziewior and Schmid [21] and the SRH recombination lifetime from Lee [22]. Two different doping dependencies for the hole mobility were considered: the majority-carrier mobility μ(maj) given by Arora et al. [19] and the suggested empirical expression of Burk and de La Torre [43] for the minority-carrier mobility μ(min). The values from [19] were used for the base region. The data of Slotboom and de Graaf [18] were used for the bandgap narrowing.

For qualitative understanding of Figs. 4.2 and 4.3, we consider a uniformly doped emitter region. Then the differential equation for $\tilde{p}(x)$ can be written as

$$\frac{d^2x}{dx^2} = \frac{\tilde{p}(x)}{L_p^{*2}} \quad , \tag{4.30}$$

where L_p^* is the complex diffusion length defined by

$$L_p^* = L_p/(1 + i\omega\tau_p)^{1/2} \quad . \tag{4.31}$$

As the frequency increases, such that $\omega\tau_p \gg 1$, the magnitude of L_p^* decreases. The current at the edge of the SCR at x_1, $j_p(x_1)$ (Fig. 4.1), starts to deviate from its low-frequency value when the slope of $\tilde{p}(x)$ at $x = x_1$ changes. Therefore, the break frequency f_B at which the small-signal admittance starts to increase from its low-frequency value

depends on the $d\bar{p}/dx$ in the low-frequency limit, which is determined by the neutral emitter width and the surface boundary condition (S_p). When the width of the neutral emitter is larger than the diffusion length, f_B is $1/\pi\tau_p$ [44]. For the short-emitter case, f_B depends on S_p and f_B is equal to $1/2\pi\tau_t$ (τ_t = transit time) for $S_p \gtrsim 10^6$ cm/s. The relation between f_B and τ_t was confirmed experimentally by Gonzalez and Neugroschel [44] and applied for the measurement of the minority-carrier diffusion coefficient [45], [46]. As S_p decreases, f_B will also decrease because the diffusion current is suppressed when S_p decreases. Therefore, the measurement of f_B for transistors with different emitter surface contacts (for example, ohmic contact and polysilicon contact) can yield an information about S_p. Figure 4.4 displays the simulated values for f_B as a function of W_E for two different values of S_p and mobility of Burk et al. [19].

Figure 4.5 displays the ratio of low-frequency small signal diffusion capacitance C defined by (4.29) to the quasi-static capacitance (C_{QSA}), which is defined as

$$C_{QSA} = \Delta Q^{(E)}/\Delta V_{BE} \quad . \tag{4.32}$$

In (4.32), $Q^{(E)}$ is the steady-state minority-carrier charge stored in the quasi-neutral emitter region. As a result of the diffusion delay due to the distributed nature of the charge transport, the small-signal capacitance is different from C_{QSA}. It is well known that for the uniform doping profile and ohmic contact at the surface the ratio is 2/3 in the narrow-diode emitter and 1/2 in the long-diode emitter [47]. These standard results agree with our results shown in Fig. 4.5.

From Fig. 4.5 we can also see that $C \simeq C_{QSA}$ for small values of S_p

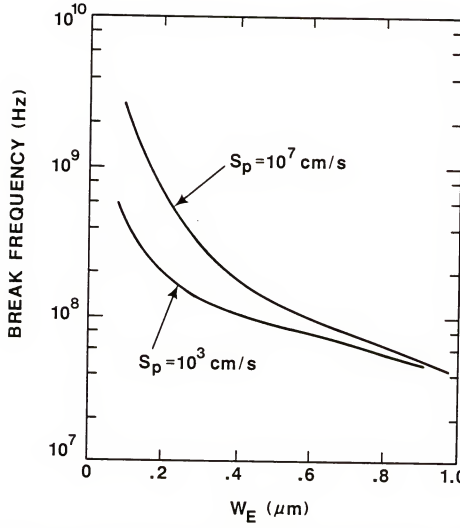

Figure 4.4 The emitter break frequency $2\pi f_B$ determined by extrapolating the high frequency range of $G/G(0) \propto f^{1/2}$ from Fig. 4.2 as a function of the quasi-neutral emitter width.

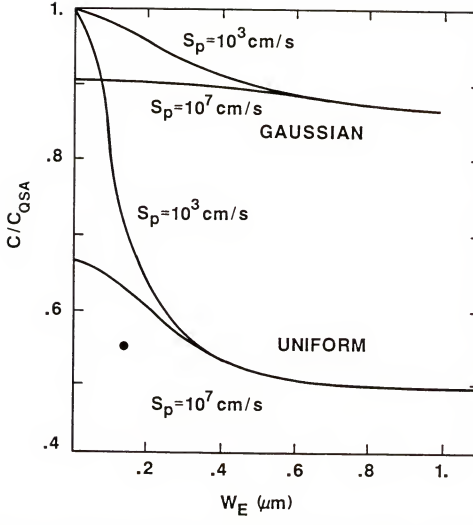

Figure 4.5 The ratio of the low-frequency small-signal capacitance to the quasi-static capacitance C_{QSA} as a function of W_E. The solid circle is for the base profile shown in Figure 4.1 with W_B = 1400 Å.

for narrow emitters for both uniform and Gaussian profiles. The Gaussian doping profile creates a retarding quasi-electric field [16] in the neutral region, which increases the C/C_{QSA} ratio in comparison with that for the uniform profile. The solid circle in Fig. 4.5 shows the ratio equal to 0.54 for the 1400 Å wide base doping profile shown in Fig. 4.1. This base doping profile yields an enhancing electric field in the quasi-neutral base region, which decrease the C/C_{QSA} ratio.

From the simulation results we can conclude that the physical origin of the difference between the small-signal and the quasi-static capacitances can be interpreted as the breakdown of the quasi-equilibrium condition within the quasi-neutral region (Chapter II). When the quasi-equilibrium condition is formed inside the quasi-neutral region, the diffusion and drift currents have nearly the same magnitude but in the opposite directions, and the resulting external current is much smaller than each component. Therefore, C approaches C_{QSA} when the magnitude of the retarding electric field increases, the quasi-neutral region width becomes smaller, and the surface recombination velocity at the contact decreases.

From the above considerations we can also conclude that the quasi-static capacitance of the space-charge region obtained from the DC simulation (Chapter V) will be very close to the small-signal capacitance of the space-charge region because in the space-charge region the quasi-equilibrium condition is nearly perfectly satisfied.

The result that $C/C_{QSA} \approx 1$ when the quasi-equilibrium condition is formed in the quasi-neutral region, can be best interpreted using the transmission-line representation of the region due to Sah [48]. Figure

4.6 shows the distributed nonequilibrium circuit for a simplified case of negligible recombination in the bulk and at the surface. In the circuit the nodal variable on top is the quasi-Fermi potential for holes v_p. For steady-state and low-frequency excitations v_p is almost position independent when the quasi-equilibrium condition exists, as was discussed in Section 2.2.3. The simplified circuit corresponding to the negligible position variation of v_p is shown in Fig 4.6 (b) where the resistances are shorted. From Fig. 4.6 (b) we obtain the small-signal capacitance as a sum of storage capacitances, $C = \Sigma C_p \Delta x = C_{QSA}$.

In Fig. 4.7 we illustrate the input impedance plotted in polar coordinates for bipolar transistors with different emitter surface recombination velocities. Note that the frequency at which the phase angle is -45° depends strongly on S_p. The -45° frequency is proportional to the ratio of input conductance and capacitance and will increase with bias because input conductance is a much stronger function of frequency than is input capacitance.

We now turn our attention to the base region. For the transistor operating in the forward-active mode, we use the common approximation that the excess hole concentration at the edge $x = x_3$ of the base-collector SCR is $\Delta p = 0$. The small signal collector current j_C and the base contribution to the base current $j_B^{(B)}$ can then be expressed as

$$j_C = j_n(x_3) = \alpha_T(\omega) j_n(x_2) \tag{4.33}$$

$$j_B^{(B)} = [1 - \alpha_T(\omega)] j_n(x_2) \quad . \tag{4.34}$$

Since the quasi-neutral base width W_B is much smaller than the DC diffusion length L_p, the base transport factor $\alpha_T(\omega = 0)$ is nearly equal to unity. We can see from (4.33) and Fig. 4.3 that the magnitude

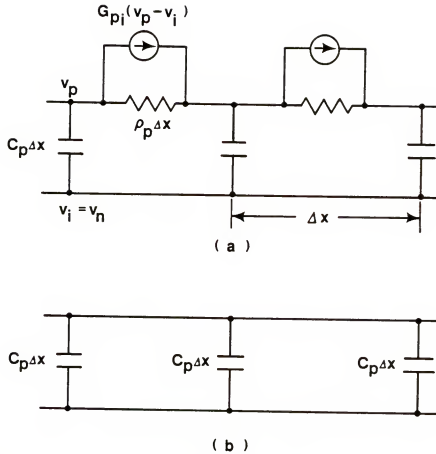

Figure 4.6 The complete distributed nonequilibrium circuit according to Sah 48 for an n-region in low injection with negligible recombination in the bulk and at surface. The definition of the circuit elements is as follows: C_p is the hole charge storage capacitance, $\sigma_p = q\mu_p P = 1/\rho p$ is the hole conductance, $G_{pi} = qJ_p/kT$ is the current generator proportional to the DC current J_p, v_p and v_n are the hole and electron electro-chemical potentials, v_i is the intrinsic potential, and x is the spatial variable. (b) Simplified circuit from (a) shorting $\rho_p \Delta x$ elements.

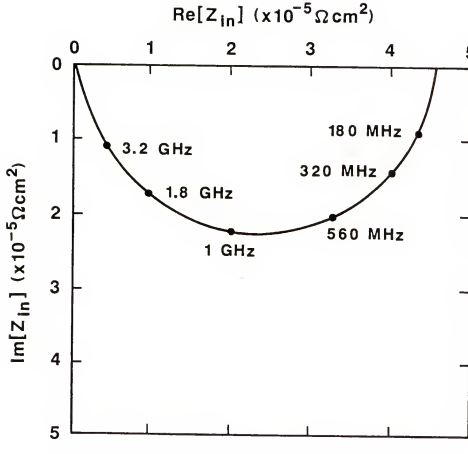

Figure 4.7 The real and imaginary part of the input impedance plotted (a) in polar coordinates. Emitter doping profile is a Gaussian with W_E = 1000 Å, $u_p = u_p(\min)$, V_{BE} = 0.85 V, and (a) $S_p = 10^3$ cm/s, (b) $S_p = 10^7$ cm/s.

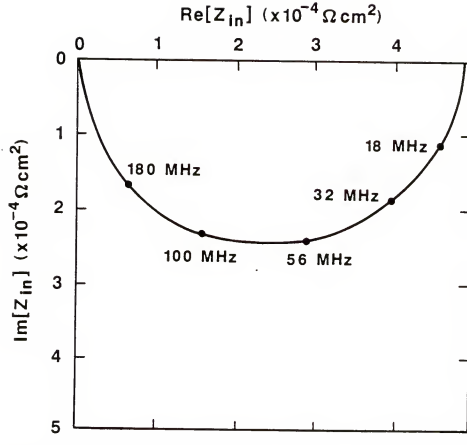
Re[Z$_{in}$] (x10^{-4} Ω cm^2)
0
1
2
3
4
5
Im[Z$_{in}$] (x10^{-4} Ω cm^2)
180 MHz
100 MHz
56 MHz
32 MHz
18 MHz

Figure 4.7 (b)

of $\alpha_T(\omega)$ decreases with increasing frequency. It is common to model the frequency dependence of α_T by a single-pole approximation including an excess phase-shift factor ωT_d [40]

$$\alpha_T(\omega) = \frac{\exp(-i\omega T_d)}{1 + i\omega/\omega_\alpha} \quad . \tag{4.35}$$

In Fig. 4.8 we display the magnitude and phase of $\alpha_T(\omega)$ for the base doping profiles shown in Fig.4.1. The broken line shows a fit to (4.35) using $T_d = 0.9$ ps and $\omega_\alpha = 35$ GHz giving excellent agreement with the accurate numerical dependence. The single-pole approximation without the excess phase shift gives a large error in phase for $f \gtrsim 10$ GHz. The factor T_d in (4.35) translates to a pulse delay of $T_d \approx 0.9$ ps in the time domain. This represents the delay due to the transport across the intrinsic base region in a bipolar transistor.

It was shown by Chen and Lindholm [49] that the diffusion delay can be represented in a conventional equivalent circuit by an inductor L in series with a resistance R. The modification of the quasi-static circuit by incorporating L will give the correct phase in the frequency domain.

In Fig. 4.9 we show the frequency dependence of common-emitter current gain β calculated at $V_{BE} = 0.85$ V. The space-charge region capacitance was calculated numerically using the quasi-static approximation and included in the calculation of β. The base doping profile is as shown in Fig. 4.1 and the Gaussian emitter profile changes from 10^{20} cm^{-3} at the surface to 10^{18} cm^{-3} at the emitter-base SCR edge. Figures. 4.9 (a) - 4.9 (d) clearly show that the conventional assumption of a frequency independent L_p predicts much larger intrinsic

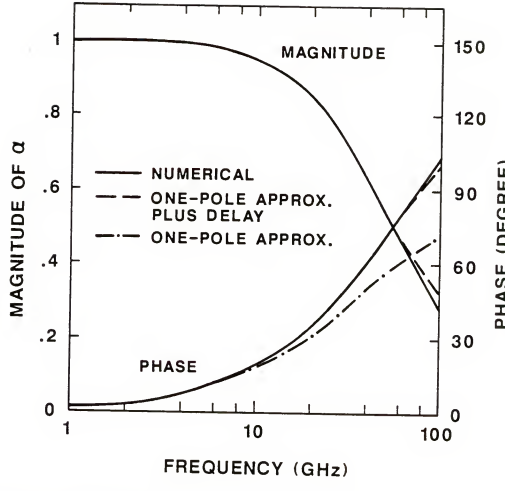

Figure 4.8 Magnitude and phase of the base transport factor α_T as a function of frequency for the base profile shown in Fig. 4.1

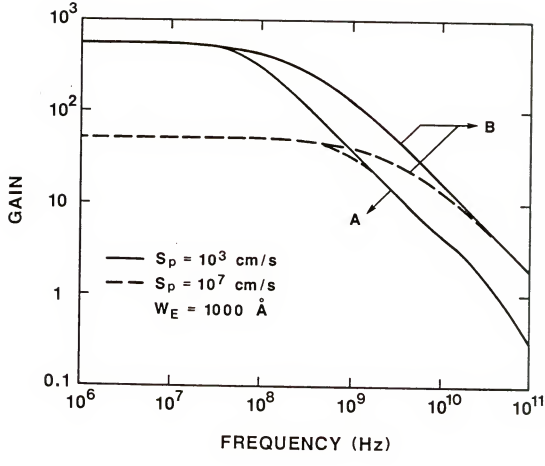

Figure 4.9 Frequency dependence of common-emitter current gain β. (a) Curves labeled A consider the frequency-dependent local minority-carrier diffusion length in the quasi-neutral emitter and base region. Curves labeled B assume frequency independent diffusion lengths. Emitter doping profile is Gaussian changing from 10^{20} cm^{-3} to 10^{18} cm^{-3}, and base profile is shown in Fig. 5.1, V_{BE} = 0.85 V. (a) $\mu_p = \mu_p$(min), W_E = 1000 Å, (b) $\mu_p = \mu_p$(min), W_E = 2000 Å, (c) $\mu_p = \mu_p$(maj), W_E = 1000 Å, (d) $\mu_p = \mu_p$(maj), W_E = 2000 Å.

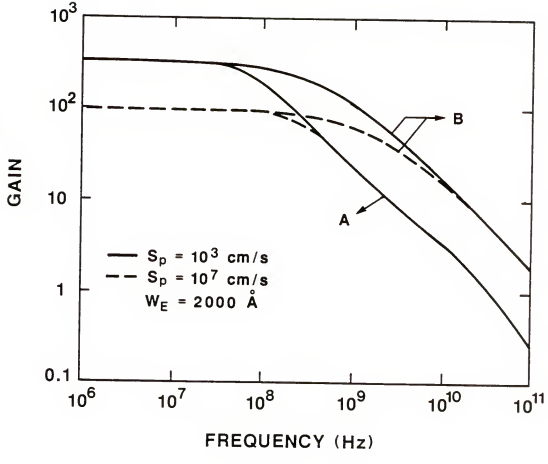
GAIN
FREQUENCY (Hz)
10^3
10^2
10
1
0.1
10^6
10^7
10^8
10^9
10^{10}
10^{11}
B
A
$S_p = 10^3$ cm/s
$S_p = 10^7$ cm/s
W_E = 2000 Å

Figure 4.9 (b)

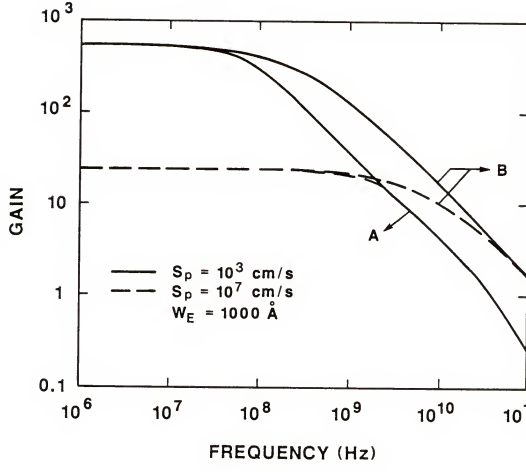
10^3
10^2
10
1
0.1
GAIN
10^6
10^7
10^8
10^9
10^{10}
10^{11}
FREQUENCY (Hz)
$S_p = 10^3$ cm/s
$S_p = 10^7$ cm/s
W_E = 1000 Å
A
B

Figure 4.9 (c)

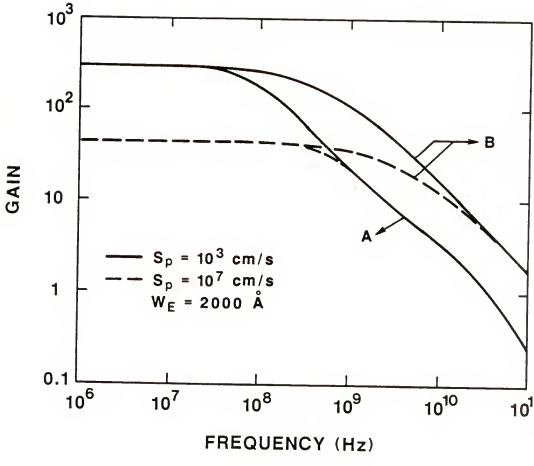
10^3
10^2
10
1
0.1
GAIN
B
A
$S_p = 10^3$ cm/s
$S_p = 10^7$ cm/s
W_E = 2000 Å
10^6
10^7
10^8
10^9
10^{10}
10^{11}
FREQUENCY (Hz)

Figure 4.9 (d)

current gain for f > 100 MHz and much larger values of the unity gain frequency f_T in comparison with the actual dependence considering transport with the frequency-dependent local L_p^*. The break frequency at f ≈ 100 MHz is the emitter effect due to the frequency-dependent L_p^*. The influence of the intrinsic base can be seen only at much higher frequencies. This influence is seen, for example, in Fig. 4.9 (a) as a second break point at f ≈ 20 GHz. Since the f_T for modern Si transistors is limited by parasitics and is about f_T ≈ 20 GHz, the influence of the intrinsic base region on f_T is negligible. The effect of the emitter, on the other hand, reduces the current gain already at f ≈ 100 MHz. It is important to note that the dependences in Fig 4.9 neglect the transit time across the base-collector SCR and the effects of parasitics.

The comparison of the identical emitters except for different surface conditions, $S_p = 10^3$ cm/s and 10^7 cm/s, shows that low S_p increases current gain in the low frequency range, but decreases the roll-off corner frequency. The values of $S_p \approx 10^3$ cm/s corresponds to emitters contacted by polysilicon [34], while $S_p \approx 10^7$ cm/s applies for metal contacts. Hence, polysilicon contacts have a beneficial effect on the current gain at low frequencies, but in the high frequency range, where both emitters become long (Fig. 4.3), the frequency response becomes identical and insensitive to the properties of surface contacts.

4.4 Summary

In this work we have developed a simple numerical method that simulates the small-signal minority-carrier transport of the injected

carriers in the quasi-neutral region. From the simulation results, we can obtain a qualitative and quantitave insight about the small-signal transport. Examples of the frequency dependence of the current gain and other parameters are shown. The results are useful and applicable for device and circuit analysis.

CHAPTER FIVE
AN ANALYTICAL STUDY OF THE P/N JUNCTION SPACE-CHARGE REGION UNDER HIGH FORWARD VOLTAGE

5.1 INTRODUCTION

The purpose of this work is to provide an insight into the behavior of the p/n junction space-charge region subjected to large forward voltage.

The characteristics of the p-n junction space-charge region have been investigated by many authors using numerical simulations or analytical approximations [1],[43],[50]-[63]. For analytical treatment, the p-n junction diode is divided into the quasi-neutral regions (QNR) and the space-charge region (SCR) or the transition region. Analytical modeling of the SCR seeks to obtain such variables as the distribution of potential, the quasi-static capacitance (C_{SCR}) due to the charge stored in the SCR and the position of the boundary between the QNR's and the SCR. This is difficult to accomplish because of the nonlinearity of the Poisson equation. One of the most useful analytical models is due to Schottky [50]. In this model it is assumed that the SCR is depleted of mobile free carriers. Outside of this region, the quasi-neutral condition is preserved; i.e., the electric field due to immobile impurity atoms is nearly fully neutralized by free electrons and holes. Schottky's model applies well under reverse bias but introduces error for forward bias conditions. Qualitatively, for reverse bias, the SCR is composed of two regions: a depletion region

and two partially screened regions. In the depletion region, we can safely neglect the free carriers and the space charge is due to the ionized impurity concentration only. Between the depletion region and the adjoining quasi-neutral regions the impurity charge is partially screened by free carriers. The validity of the depletion approximation requires that the total charge in the depletion region be much larger than that in the partially screened regions.

For reverse or small bias voltage, the depletion region occupies most of the SCR. The charge in the depletion region then becomes dominant and the depletion approximation becomes reasonably accurate. Under large forward voltage the depletion region width becomes narrower and the free electrons and holes in the SCR cannot be neglected.

In general, C_{SCR} is composed of two components: a capacitance C_C due to the change of the stored space-charge and another component C_M from the change of mobile electrons and holes in the SCR (see Eq (39)). Numerical simulations show that C_C increases with forward bias voltage until it reaches a maximum and then it decreases rapidly while C_M increases monotonically with forward voltage. In the Schottky model, the C_{SCR} diverges to infinity when the applied forward voltage is equal to the built-in potential.

There have been many efforts to improve the simple Schottky model analytically [43]-[62] by including the effects of stored free carriers in the SCR. The behavior of the p-n junction transition region at high forward voltage was modeled by several authors [59]-[62]. Morgan and Smits [59] proposed a "neutral approximation" for the linearly graded junction. In the neutral approximation, assuming that the space charge density is zero in the whole transition region. This model becomes

accurate as the forward bias voltage increases. Lindholm [60] proposed a "p-i-n diode" model, where the SCR is regarded as the i (intrinsic) region of a p-i-n structure which is excited in the sense that the large forward voltage creates electron and hole densities orders of magnitude larger than those in equilibrium.

In this work, we analyze the transition region of the p-n junction under large forward bias voltage. It will be shown that when the high injection condition prevails in the QNR's adjoining the SCR, the Poisson equation can be linearized and solved analytically. From the solutions we obtain a detailed physical insight about the SCR behavior under high forward bias voltages not afforded by other models. Accurate analytical solutions obtained, such as C_{SCR} and the position of the SCR edges, are intended to be useful for device modeling and the circuit analysis of p-n junction devices.

The definitions of the distribution of the externally applied bias voltage in the p-n junction and the appropriate boundary conditions are reviewed in Section 5.2. In Section 5.3 properties of the SCR under high level injection conditions for a symmetric step junction are investigated, interpreted physically and compared with the numerical simulation. An analysis for an exponential doping profile which includes the linearly graded junction as a special case follows in section IV.

5.2 Basic Concepts

The Poisson equation that describes the potential distribution in the SCR in the absence of trapped charge is

$$\frac{d^2\psi}{dx^2} = -\frac{\rho}{\epsilon_s} = -\frac{e}{\epsilon_s}[p(x) - n(x) + N(x)] \quad , \tag{5.1}$$

where ψ is the electrostatic potential, ρ is the space-charge density, e is the electron charge, p and n are electron and hole concentrations respectively, and N(x) is the net ionized impurity concentration which is positive for donor and negative for acceptor impurity atoms:

$$N(x) = N_D(x) - N_A(x) \quad . \tag{5.2}$$

In terms of the electron and hole electrochemical potentials ϕ_n and ϕ_p, the assumed nondegenerate electron and hole concentrations can be expressed as

$$p = n_i \exp[(\phi_p - \psi)/V_T] \tag{5.3}$$

$$n = n_i \exp[(\psi - \phi_n)/V_T] \tag{5.4}$$

where n_i is the intrinsic carrier concentration and V_T is the thermal voltage. Using the electrochemical potentials, one can express electron and hole current as

$$J_n = -en\mu_n \frac{d\psi}{dx} + eD_n \frac{dn}{dx} = -e\mu_n n \frac{d\phi_n}{dx} \tag{5.5}$$

$$J_p = -ep\mu_p \frac{d\psi}{dx} - eD_p \frac{dp}{dx} = -e\mu_p p \frac{d\phi_p}{dx} \tag{5.6}$$

In (5.5) and (5.6), the Einstein relations for nondegenerate carriers are used.

We consider a p-n junction diode connected to external voltage source by the ohmic contacts at $x = W_n$ and $x = W_p$ (Fig. 5.1). The diode

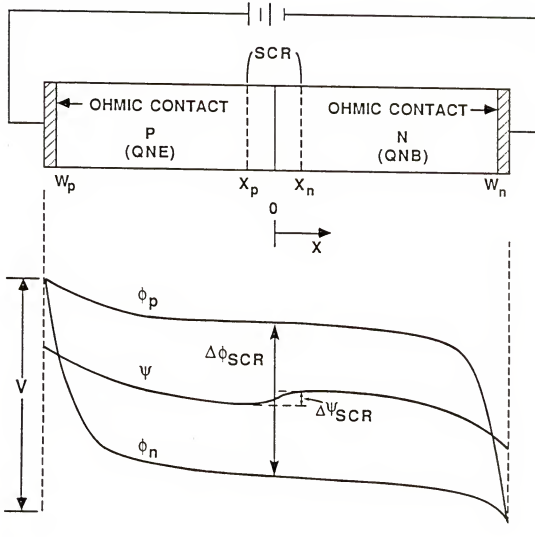

Figure 5.1 Schematic of a p-n junction with the electrostatic potential and electro-chemical potentials as functions of positions.

can be subdivided into the three regions, quasi-neutral emitter region (QNE), quasi-neutral base region (QNB), and the space-charge region (SCR):

$$\begin{aligned} &\text{QNE: } 0 \approx |\rho(x)| \ll |eN(x)| \ , && W_n \geq x \geq x_n \\ &\text{SCR: } (X) \neq 0 \ , && x_n \geq x \geq x_p \\ &\text{QNB: } 0 \approx |\rho(x)| \ll |eN(x)| \ , && x_p \geq x \geq W_p \ . \end{aligned} \tag{5.7}$$

The space-charge density in a quasi-neutral region tends to increase as the gradient of the net impurity concentration increases. When the doping gradient is severe, as may be true for a distributed high-low junction, the quasi-neutrality condition expressed in (5.7) may be violated. We omit consideration of this possibility in this study. Figure 5.1 also shows the schematic distribution of ϕ_p, ϕ_n, and Ψ. We also assume ohmic contacts at $x = W_p$ and $x = W_n$:

$$\phi_p(W_p) = \phi_n(W_p) \tag{5.8}$$

$$\phi_p(W_n) = \phi_n(W_n) \ . \tag{5.9}$$

The applied voltage V is equal to the difference of the electrochemical potentials between the ohmic contacts:

$$V = \phi_p(W_p) - \phi_n(W_n) \ . \tag{5.10}$$

Marshak and van Vliet [64] discussed the distribution of the applied potential inside the p-n diode. The difference of the intrinsic potential between ohmic contacts can be expressed as

$$\psi(W_n) - \psi(W_p) = \int_{W_p}^{W_n} \frac{d\psi}{dx}\, dx \quad . \tag{5.11}$$

Using (5.4), one can write (5.11) as

$$\int_{W_p}^{W_n} \frac{d\psi}{dx} = \int_{W_p}^{W_n} d\phi_n + V_T \int_{W_p}^{W_n} d\, \ln\left(\frac{n}{n_i}\right) \quad . \tag{5.12}$$

The first term of the right side in (5.12) is the negative of the external voltage and the second term is the equilibrium electrostatic potential difference between ohmic contacts. From (5.11) and (5.12), we can see that the electrostatic potential difference is equal to the electrostatic potential difference in equilibrium minus voltage V. From these facts, Marshak and van Vliet defined the distribution of the applied external voltage inside the p-n diode as follows:

$$V = V_{QNE} + V_{SCR} + V_{QNB} \quad , \tag{5.13}$$

where each term is defined as

$$V_{QNE} = [\psi_0(x_{p0}) - \psi_0(W_p)] - [\psi(x_p) - \psi(W_p)]$$

$$V_{QNB} = [\psi_0(W_n) - \psi_0(x_{n0})] - [\psi(W_n) - \psi(x_n)]$$

$$V_{SCR} = [\psi_0(x_{n0}) - \psi_0(x_{p0})] - [\psi(x_n) - \psi(x_p)] \quad , \tag{5.14}$$

where the subscript zero means equilibrium values.

For analytical study of the SCR, we assume the following boundary conditions:

(a) The charge neutrality condition at $x = x_n$ and $x = x_p$ can be expressed as

$$n(x_n) \approx N_D(x_n) + p(x_n) \tag{5.15}$$

$$p(x_p) \approx N_A(x_p) + n(x_p) \tag{5.16}$$

(b) The electrochemical potentials are nearly flat throughout the SCR, as shown in Fig. 5.1 :

$$\frac{d\phi_n}{dx} \approx \frac{d\phi_p}{dx} \approx 0 \quad \text{for } x_p \le x \le x_n \quad . \tag{5.17}$$

The change of the electrochemical potentials across the SCR is given by

$$\phi_p(x_n) - \phi_p(x_p) = -\int_{x_p}^{x_n} \frac{J_p}{ep\mu_p}\, dx \tag{5.18}$$

$$\phi_n(x_n) - \phi_n(x_p) = -\int_{x_p}^{x_n} \frac{J_n}{en\mu_n}\, dx \quad . \tag{5.19}$$

J_n and J_p in (5.18) and (5.19) are determined by the doping profile and the geometry of the QNR's. Van der Ziel [65] discussed the validity of the Boltzmann boundary conditions related to (5.17) under low level injection for a step junction and concluded that they are accurate if the SCR width is much smaller than the characteristic length of the QNR expressed as

$$\left[\left(\frac{d}{dx} \ln p\right)\Big|_{x_n}\right]^{-1} \quad \text{and} \quad \left[\left(\frac{d}{dx} \ln n\right)\Big|_{x_p}\right]^{-1} \quad .$$

The characteristic length is the minority-carrier diffusion length L_n and L_p for a long diode or the width of the QNR for a short diode with uniformly doped QNR. The same conclusion can be obtained for moderate

or high injection case provided that the current is proportional to the injected carrier concentration.

5.3 Symmetric Step Junction Under High Forward Bias Voltage

Consider a symmetric step junction with the following doping profile:

$$N(x) = N_0 \quad \text{N type } (x \geq 0)$$

$$N(x) = -N_0 \quad \text{P type } (x \leq 0) \quad . \tag{5.20}$$

Choosing the potential reference so that $\psi(0) = 0$, the electrostatic potential is an odd function of x due to the symmetry of the doping profile. The electrostatic potential in the QNR can be calculated by applying the quasi-neutrality condition ($|\rho| \ll en$ and $|\rho| \ll ep$) for $x \geq x_n$:

$$(x = x_n) = V_T \ln \left[-\frac{1}{2 n_i \exp(\Delta\phi_{SCR}/2V_T)} + \right.$$

$$\left. + \left\{ \left(-\frac{1}{2 n_i \exp(\Delta\phi_{SCR}/2V_T)} \right)^2 + 1 \right\}^{1/2} \right] \quad . \tag{5.21}$$

where $\Delta\phi_{SCR}$ is the difference between the hole and electron electrochemical potentials. Therefore, by symmetry,

$$\Delta\psi_{SCR} = 2\,\psi(x=x_n) \quad , \tag{5.22}$$

where $\Delta\psi_{SCR} = \psi(x_n) - \psi(x_p)$. The built-in potential in equilibrium is

$$\Delta\psi_{SCR0} = 2V_T \ln (N_0/n_i) \tag{5.23}$$

and

$$V_{SCR} = \Delta\Psi_{SCR0} - \Delta\Psi_{SCR}$$

$$= \Delta\phi_{SCR} - 2V_T \ln \left[\frac{1}{2} + \left(1 + \frac{4n_i^2}{N_0^2} \exp\left(\Delta\phi_{SCR}/V_T\right)\right)^{1/2}\right] . \qquad (5.24)$$

When the p-n junction is in low injection, the injected minority carrier concentration at the edge of QNR is much smaller than the doping concentration

$$p(x_n) = (n_i^2/N_0) \exp\left(\Delta\phi_{SCR}/V_T\right) \ll N_0 \quad . \qquad (5.25)$$

Hence, we can conclude that $V_{SCR} = \Delta\phi_{SCR}$ in low injection.

As the bias increases, the majority carrier concentration is modulated significantly and V_{SCR} become smaller than $\Delta\phi_{SCR}$. In high injection,

$$n(x_n) \approx p(x_n) \approx n_i \exp\left(\Delta\phi_{SCR}/2V_T\right) \geq N_0 \quad , \qquad (5.26)$$

$$\Delta\Psi_{SCR} \approx V_T \frac{N_0}{n_i \exp\left(\Delta\phi_{SCR}/2V_T\right)} \leq V_T \quad . \qquad (5.27)$$

From (5.23) and (5.27), we can see that the condition of high level injection for a symmetric step junction implies that the separation of the electron and hole electrochemical potentials across the SCR is larger than the equilibrium built-in potential. Under condition (5.27), the Poisson equation can be linearized by approximating $\exp(x) \approx 1 + x$:

$$\frac{d^2\psi}{dx^2} = -\frac{e}{\epsilon_s}\left\{N_0 - 2n_i \exp\left(\Delta\phi_{SCR}/2V_T\right)\frac{\psi}{V_T}\right\} \quad , \tag{5.28}$$

where $\phi_p = -\phi_n = \Delta\phi_{SCR}/2$.

The general solution of (5.28) is

$$\psi(x) = V_T \frac{N_0}{2n_i \exp\left(\Delta\phi_{SCR}/2V_T\right)} + A \exp(kx) + B \exp(-kx) \quad , \tag{5.29}$$

where

$$k = (1/L_i) \exp\left(\Delta\phi_{SCR}/4V_T\right) \tag{5.30}$$

and

$$L_i = (\epsilon_s V_T/2ne_i)^{1/2} \tag{5.31}$$

is the intrinsic screening length.

Since $\psi(x)$ should not diverge at infinity in (5.29), $A = 0$.

Inserting $\psi(0) = 0$, it yields

$$\psi(x) = V_T \frac{N_0}{2n_i \exp\left(\Delta\phi_{SCR}/2V_T\right)} \{1 - \exp(-kx)\} \quad . \tag{5.32}$$

The charge density $\rho(x)$ can be calculated using (5.32):

$$\rho(x) = eN_0 \exp(-kx) \quad . \tag{5.33}$$

If we define the SCR edge at the point where $|\rho(x)/N_0| = 0.1$, then

$$W_{SCR} = 2 (\ln 10) L_i \exp\left(-\Delta\phi_{SCR}/4V_T\right) \quad . \tag{5.34}$$

Except for the factor, ln10, this is equivalent to the general expression derived by Lindholm [60] when it is applied to the general

case of a symmetric step junction. According to (5.34), W_{SCR} is independent of doping concentration in high injection and shrinks to zero exponentially with $\Delta\phi_{SCR}$.

The above results can be explained qualitatively as follows. When the SCR is highly forward biased, the change of the electrostatic potential across the SCR is smaller than thermal voltage. In this limit, n and p are nearly independent of x:

$$n \approx p \approx n_1 \exp(\Delta\phi_{SCR}/2V_T) \quad . \tag{5.35}$$

When the mobile free carrier concentration is independent of x, the Debye-Huckel screening model is applicable [66] and the mobile free carriers will screen the charged impurity atoms with a screening length:

$$L_s = [\epsilon_s V_T/(p + n)e]^{1/2} \quad . \tag{5.36}$$

Meanwhile, the application of the Debye-Huckel theory in the low injection case gives a significant error due to the nonuniform carrier distribution, as discussed by Shirts and Gordon [63]. Figure 5.2 displays the distribution of the space charge in the SCR for the symmetric junction with $N_0 = 10^{17}$ cm^{-3} calculated from (5.33) and compared with the numerical simulation at various forward bias voltages. As discussed before, L_s is the screening length based on the assumption (5.35), which is accurate only near x = 0; as x increases, p < n. Recall that the pn product is independent of x in the SCR; the screening length, which is inversely proportional to $(p + n)^{1/2}$, decreases as x increases. Therefore, around the edge of the SCR the impurity atoms are screened more strongly than expected from the

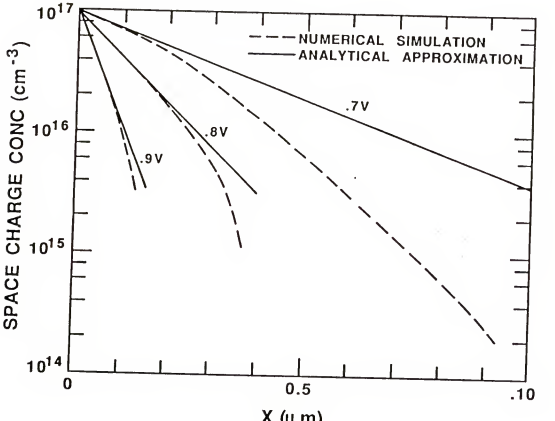

Figure 5.2 Numerical simulation results of space-charge concentration compared with the analytical approximations. Doping profile is a symmetric step junction with $N_0 = 10^{17}$ cm^{-3}.

analytical approximation. Therefore the analytical approximation (5.33) overestimates the space-charge concentration for large x.

The quasi-static capacitance of the p-n diode is defined as [1]

$$C_{QSA} = \frac{d}{dV}\int_{W_p}^{W_n} e(p - p_0)\,dx = \frac{d}{dV}\left[\int_{W_p}^{x_p} e(p - p_0)\,dx + \int_{x_n}^{W_n} e(p - p_0)\,dx + \int_{x_p}^{x_n} e(p - p_0)\,dx\right] \quad , \tag{5.37}$$

where p_0 is the equilibrium hole concentration. The sum of the first and the second terms in the right side of (5.37) is defined as the diffusion capacitance C_D which arises from the change of the stored minority-carriers in the quasi-neutral regions. The third term is the contribution of the SCR. To define the C_{SCR} independently of the doping profile and the geometry of the QNR, we define the C_{SCR} as

$$C_{SCR} = \frac{d}{d(\Delta\phi_{SCR})}\int_{x_p}^{x_n} e(p - p_0)\,dx \quad . \tag{5.38}$$

We can decompose C_{SCR} into two parts:

$$C_{SCR} = C_C + C_M = \frac{d}{d(\Delta\phi_{SCR})}\int_0^{x_n} \rho\,dx + \frac{d}{d(\Delta\phi_{SCR})}\left(\int_0^{x_n} ep\,dx + \int_{x_p}^{0} en\,dx\right) . \tag{5.39}$$

The first term on the right side of (5.39) is due to the change in the stored charge within the SCR. We call this term the charge density capacitance (also called depletion capacitance in the literature). The sum of the second and the third terms in (5.39) results from the

minority electron and hole accumulation in the SCR, and will be designated by C_M. For reverse and small forward bias voltage C_C dominates. For large forward bias voltage, C_D and C_M become more significant and larger than C_C.

An expression for C_C follows from (5.33):

$$C_C(\Delta\phi_{SCR} \to \infty) \approx \frac{eN_0L_i}{4V_T} \exp\left(-\Delta\phi_{SCR}/4V_T\right) \quad . \tag{5.40}$$

In Fig. 5.3 we compare the analytical approximations (5.40) and (5.32) for C_C and C_M with the numerical simulations. The doping profile is a symmetrical step junction with $N_0 = 10^{17}$ cm^{-3}. The simulation results show that C_C has a maximum at $\Delta\phi_{SCR} = 0.74$ Volt which is about 0.08 Volt smaller than the equilibrium contact potential. At large forward voltage C_M is proportional to exp $(\Delta\phi_{SCR}/4V_T)$ as expected from the p-i-n model [60].

5.4 Exponential and the Linearly-Graded Junction

The doping profile for a linearly-graded junction can be expressed as

$$N(x) = Ax \quad . \tag{5.41}$$

Let the potential reference be at $x = 0$. Then $\Psi(x)$ has the following asymptotic form in the quasi-neutral region

$$\Psi_{QNR}(x) = V_T \sinh^{-1} \frac{Ax}{2n_i \exp\left(\Delta\phi_{SCR}/2V_T\right)} \quad . \tag{5.42}$$

As in the case of the symmetric step junction, the Poisson equation can

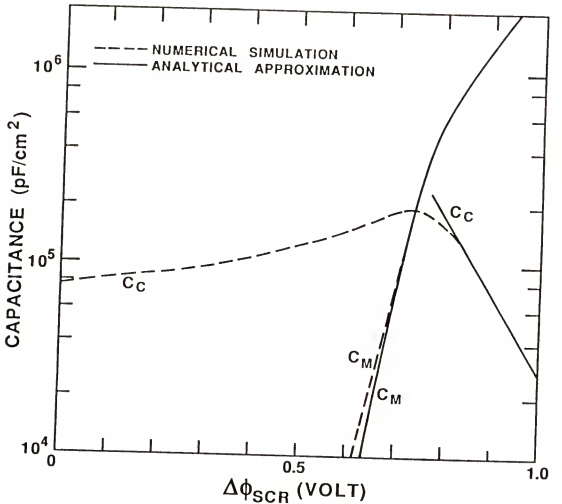

Figure 5.3 Numerical simulation results of C_{SCR} compared with the analytical approximation. Doping profile is a Symmetric step junction with $N_0 = 10^{17}$ cm^{-3}.

be linearized when high forward bias voltage is applied. It is difficult, however, to obtain an analytical solution of the linearized Poisson equation that satisfies the boundary conditions. To overcome this difficulty, we consider the following doping profile:

$$N(x) = U\,[1 - \exp(-\alpha x)] \quad , \quad x \geq 0$$
$$N(-x) = -N(x) \quad , \quad x \leq 0 \quad . \tag{5.43}$$

In (5.43), α can be interpreted as the junction stiffness which is infinite for the symmetric step junction. The linearly-graded doping profile can be approximated by taking the limit of (5.43) such that $\alpha \to 0$ while $U\alpha = A$.

The linearized Poisson equation for the doping profile of (5.43) has a general solution

$$\Psi(x) = \frac{eU}{\epsilon_s k^2} - \frac{eU}{\epsilon_s(k^2 - \alpha^2)} \exp(-\alpha x) + B\, e^{kx} + C\, e^{-kx} \quad , \tag{5.44}$$

where B and C are arbitrary constants and k is given by (5.30). Since $\Psi(x)$ should be finite at infinity, $B = 0$. We can determine C from $\Psi(0) = 0$. The results are

$$\Psi(x) = \frac{eU}{\epsilon_s}\left\{ \frac{\alpha^2}{(k^2 - \alpha^2)k^2} \exp(-kx) - \frac{1}{(k^2 - \alpha^2)} \exp(-\alpha x) + (1/k^2) \right\} \quad , \tag{5.45}$$

$$\rho(x) = eU \frac{\alpha^2}{k^2 - \alpha^2} \left\{ \exp(-\alpha x) - \exp(-kx) \right\} \tag{5.46}$$

$$Q_{SCR} = \int_0^{\infty} \rho(x)\, dx = \frac{eU\alpha}{k(k+\alpha)} \quad . \tag{5.47}$$

Equation (5.46) implies that the normalized space charge concentration $\rho(x)/U$ is independent of U and depends on α and k which are related to the junction stiffness and the applied forward voltage. The charge density $\rho(x)$ has two peaks at $x = \pm (1/\alpha - k) \ln (\alpha/k)$. When α decreases, the magnitude of the peak concentration becomes smaller and eventually flattens out. The role of k in decreasing the normalized peak concentration becomes more significant and is determined by the competition between the junction stiffness and the applied voltage, whose role is to supply the free carriers into the SCR that try to neutralize the discreteness in the doping profile.

We now turn to the linearly-graded junction. In this limit, $\alpha \to 0$, $U \to \infty$, $U\alpha \to A$, and $\rho(x)$ is uniform throughout the region as predicted by (5.46). In this case $\rho(x)$, Q_{SCR}, and C_C can be expressed as

$$\psi(x) = \frac{eA}{\epsilon_s k^2} x \tag{5.48}$$

$$Q_{SCR} = eA/k^2 \tag{5.49}$$

$$C_C = \frac{1}{4} \frac{\epsilon_s}{n_1} A \exp(-\Delta\phi_{SCR}/2V_T) \quad . \tag{5.50}$$

Figure 5.4 shows the numerical simulation results of the space-charge concentration as a function of $\Delta\phi_{SCR}$ for the linearly-graded junction with $A = 10^{22}$ cm^{-4} and 10^{24} cm^{-4}. We can see that as $\Delta\phi_{SCR}$ increases the peak charge concentration decreases and spreads out as expected.

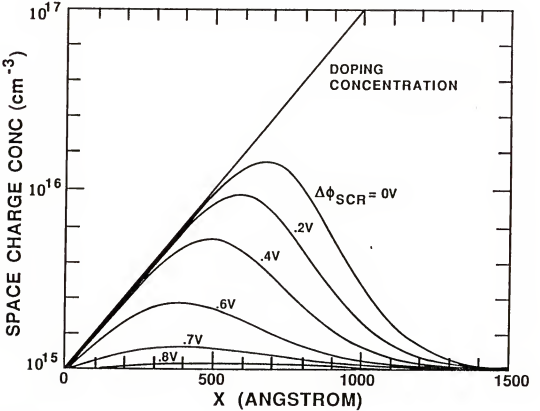

Figure 5.4 Numerical simulation results of space-charge concentration compared with (a) the analytical approximations. Doping profile is a linearly graded junction. (a) A = 10^{22} cm^{-4}. (b) A = 10^{24} cm^{-4}.

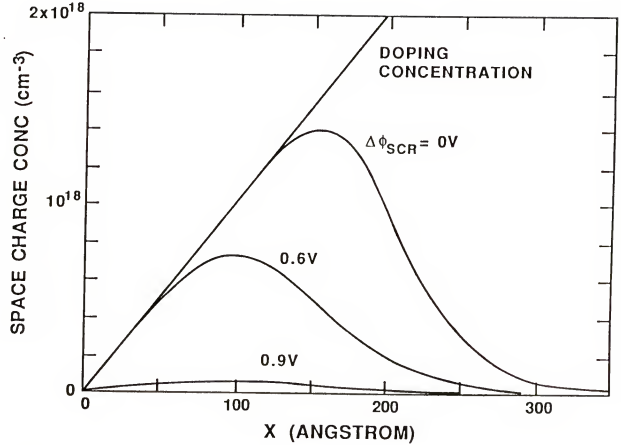
2x10^18
10^18
0
SPACE CHARGE CONC (cm^-3)
DOPING
CONCENTRATION
Δφ_SCR = 0V
0.6V
0.9V
0
100
200
300
X (ANGSTROM)

Figure 5.4 (b)

For $\Delta\phi_{SCR} > 0.7$ Volt ($A=10^{22}$ cm^{-4}) and about 0.85 Volt ($A=10^{24}$ cm^{-4}), the space-charge region almost disappears. As a test of our analytical approximation for the behavior of the linearly graded junction, we compare C_C expressed in (5.50) with the numerical simulation in Fig. 5.5.

Morgan and Smits [59] extended Shockley's "neutral approximation" [1], which is valid for gradually changing doping profiles in equilibrium, to study the behavior of the linearly-graded junction under large forward bias. The neutral approximation assumes that the charge neutrality exists everywhere. Therefore as expressed in (5.42) is assumed everywhere. This approximation is valid only when the SCR collapses, at approximately $K \approx 1$, where [59]

$$K = \frac{AL_i}{2n_i} \exp\left(-3\Delta\phi_{SCR}/4V_T\right) \quad . \tag{5.51}$$

As an extension of the work of Morgan and Smits, first order corrections to $\Psi(x)$ in the neutral approximation ($\Psi(x) = \Psi_{neutral} + \Delta\Psi$) are performed using the linearized Poisson equation in $\Psi(x)$. Fig. 5.6 shows these corrections and emphasizes the accuracy of the neutral approximation for large applied voltages and hence large values of $\Delta\phi_{SCR}$. This result is an expected one since the linearly graded junction has the least junction stiffness. Thus for a linearly graded junction, the neutral approximation becomes more accurate than it is for other types of p-n junction.

5.5 DISCUSSION

The general behavior of the space-charge region under high forward voltages was studied quantitatively by linearizing the Poisson equation. We have obtained a qualitative understanding by making

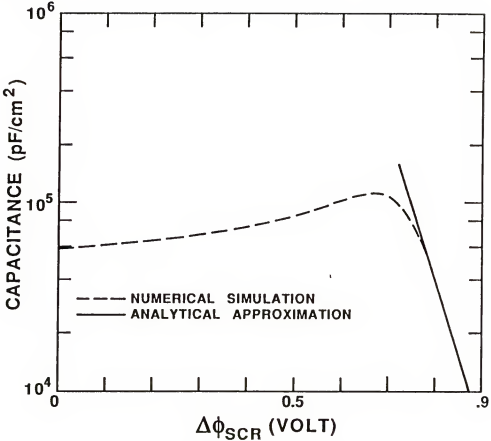

Figure 5.5 Numerical simulation results of C_C compared with the analytical approximation. (a) Doping profile is a linearly graded junction. (a) A = 10^{22} cm^{-4}, (b) A = 10^{24} cm^{-4}.

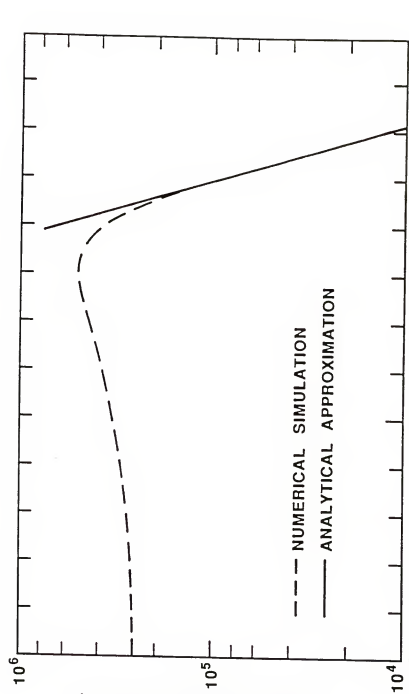
CAPACITANCE (pF/cm-3)
10^6
10^5
10^4
0
0.5
1.0
$\Delta\phi_{SCR}$ (VOLT)
NUMERICAL SIMULATION
ANALYTICAL APPROXIMATION

Figure 5.5 (b)

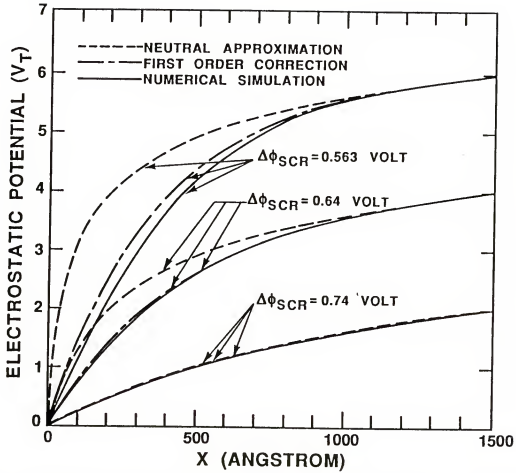

Figure 5.6 Comparison of electrostatic potential distribution for the neutral approximation, first-order correction to the neutral approximation, and the numerical simulations at various bias voltages. Doping profile is a linearly graded junction. (a) A = 10^{22} cm^{-4}, (b) A = 10^{24} cm^{-4}.

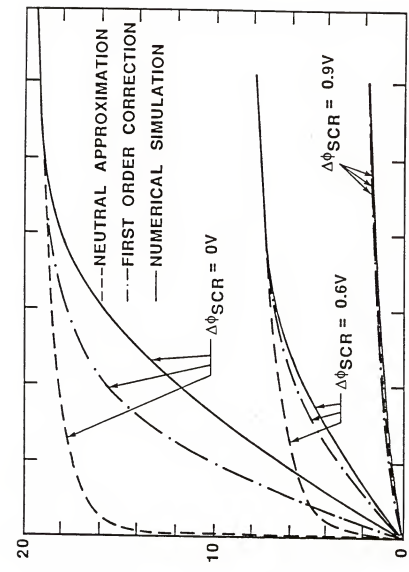
ELECTROSTATIC POTENTIAL (V_t)
20
10
0
0
100
200
300
X (ANGSTROM)
NEUTRAL APPROXIMATION
FIRST ORDER CORRECTION
NUMERICAL SIMULATION
$\Delta\phi_{SCR}$ = 0V
$\Delta\phi_{SCR}$ = 0.6V
$\Delta\phi_{SCR}$ = 0.9V

Figure 5.6 (b)

calculations that explore the competition between the junction stiffness parameter α and the number of free carriers in the space-charge region. The approach used in this paper can be extended to the junctions having arbitrary doping profiles.

In the interpretations of the present work and its extensions, however, the following precautions are noted:

1) Quantum limit.

As the forward bias voltage increases, the characteristic length expressed in (30) and W_{SCR} decrease, approaching the quantum limit where the classical point particle concept cannot be applied. In this limit, the distribution function for electrons and holes should be solved from quantum mechanics. The critical length beyond which the treatment presented here is invalid can be roughly estimated by setting $W_{SCR} \approx$ thermal de Broglie wavelength:

$$\lambda = h/p \approx 60 \text{ Å} \quad \text{(at room temperature for silicon)} \quad .$$

2) Carrier injection conditions.

In our study we have confined our attention to the SCR only, assuming flat electron and hole quasi-Fermi potentials. The injected carriers can be supplied from outside in several ways: electrical excitation through ohmic contacts, optical excitation, or injection and transport from other junctions (for example, the base-collector junction in bipolar junction transistors). When the carriers are supplied through ohmic contacts, the quality of the ohmic contacts as well as the ohmic voltage drop across the QNR's should be taken into account.

CHAPTER SIX
STUDY OF THE LATERAL P-N-P TRANSISTORS USING TWO-DIMENSIONAL DEVICE SIMULATOR

6.1 Introduction

The lateral p-n-p transistors are widely used in analog and digital circuits together with the vertical n-p-n transistors. Compared with the vertical n-p-n transistors the DC, AC , and the transient characteristics of the lateral p-n-p transistors are far worse. This is mainly because the lateral diffusion of impurity atoms and the charge storage under the emitter and collector pocket. In general, the average neutral base width is larger than that of the n-p-n transistor due to the lateral diffusion of impurity atoms and the low epitaxial base concentration. As a result, the delay time of the lateral p-n-p transistor is determined by the base charge storage time of the neutral base region which will be defined in Section 6.2.

In this work we investigate numerically the characteristics of the lateral p-n-p transistor fabricated with the process conditions designed for n-p-n transistors. The speed limit of the submicron lateral p-n-p transistors are studied using FIELDAY program [67].

6.2 Analysis

Fig. 6.1 shows the cross-section of the lateral transistor to be studied in this work. The physical parameters and the simulation results are summarized in Table 6.1. The computer program includes the heavy doping effects, such as bandgap narrowing and the Auger

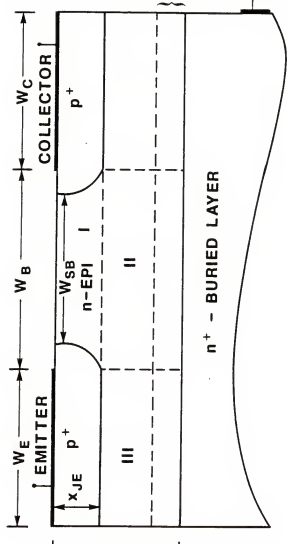

Figure 6.1 Schematic diagram of a lateral p-n-p transistor under study.

Table 6.1 Summary of the simulation results

Device number	W_B (μm)	X_{JE} (μm)	W_E (μm)	X_{epi} (μm)	τ_{SB} (μm)	β
D-1	2.0	0.3	2.0	1.3	2.7	6.1
D-2	1.5	0.3	1.5	1.3	1.4	11
D-3	1.0	0.3	1.0	1.3	0.57	27
D-4	1.0	0.3	0.5	1.3	0.38	45
D-5	1.0	0.3	1.0	0.8	0.33	20
D-6	1.0	0.3	0.5	0.8	0.23	35
D-7	1.225	0.3	1.0	0.8	0.55	13
D-8	1.375	0.5	1.0	1.0	0.54	23
D-9	1.525	0.7	1.0	1.2	0.53	35
D-10	1.75	1.0	1.0	1.5	0.5	0.54
D-11	2.125	1.5	1.0	2.0	0.59	71
D-12	1.225	0.3	1.0	0.6	0.38	8.1
D-13	1.375	0.5	1.0	0.8	0.36	18
D-14	1.525	0.7	1.0	1.0	0.36	29
D-15	1.75	1.0	1.0	1.3	0.35	48
D-16	2.125	1.5	1.0	1.8	0.45	65

Epi concentration is 2×10^{16} cm^{-3}.

Emitter and collector surface concentration is 5×10^{19} cm^{-3} and assumed to be Gaussian.

Transition region distance between the epi and buried layer was assumed to be 0.3 μm.

Doping concentration in the buried layer is assumed to be 5×10^{19} cm^{-3}.

recombination. Gaussian doping profiles are assumed in the emitter and the collector regions, where the lateral straggles due to the lateral impurity diffusion are assumed to be 75% of the vertical straggles. The epi-buried layer transition thickness caused by the autodoping is assumed to be 0.3 μm.

For the qualitative understanding of the numerical results the following simple analytical approximation for the collector current in the forward active mode is useful [68]

$$I_C \simeq \frac{qn_i^2 D_p}{N_{epi}} [\exp (qV_{EB}/kT) - 1] \left[\frac{(X_{epi} - X_{JE})}{W_B} + \frac{X_{JE}}{W_B^*} \right] , \quad (6.1)$$

where W_B^* is the average neutral base width in region I (Fig. 6.1), and the other parameters have their usual meanings. The base current is composed of three components

$$I_B = I_B^{(e)} + I_B^{(bl)} + I_B^{(epi)} , \quad (6.2)$$

where $I_B^{(e)}$ is the contribution from the transport of electrons injected into the quasi-neutral emitter region, $I_B^{(bl)}$ is from the bulk recombination in the buried layer, and $I_B^{(epi)}$ is bulk recombination in the epi layer. Numerical simulation results show that the main contribution to the base current is $I_B^{(e)}$ for devices shown in Table 6.1. For shallow emitters, $I_B^{(e)}$ can be approximated as:

$$I_B^{(e)} \simeq \frac{qn_i^2}{N_{Aeff}} [\exp (qV_{EB}/kT) - 1] \frac{W_E}{X_{JE}} , \quad (6.3)$$

where N_{Aeff} is the effective doping concentration that includes the effects of the bandgap narrowing.

According to the charge control model [69], the base charge

storage time can be calculated using a quasi-static method. The emitter-collector time constant in the forward-active mode is defined as $\Delta Q_B/\Delta I_C$, where Q_B is the minority hole charge stored in the base region. The base charge storage time τ_{SB} is the emitter-collector time constant at $1/I_C \rightarrow 0$. When the transistor is in saturation mode, emitter-base time constant can be defined as $\Delta Q_B/\Delta I_B$ similarly.

Fig. 6.2 displays the emitter-collector time constant for transistors with different lateral dimensions. The rapid increase of the time constant for large I_C is due to the high-injection effects and the series resistance. Fig. 6.3 shows the dependence of τ_{SB}, extrapolated from Fig. 6.2 and the DC current gain, on the scaling in the lateral dimension. The minimum W_B required to prevent the punch-through for the base-collector reverse bias of 5 Volts is slightly less than 1.0 μm for the epi concentration $N_{epi} = 2$ E16 cm^{-3} and $X_{JE} = 0.3$ μm.

With the lateral scaling, $W_E \rightarrow \alpha W_E$, $W_C \rightarrow \alpha W_C$, and $W_B \rightarrow \alpha W_B$, where α is the scaling constant. The stored hole charge in the base region is then approximately proportional to α. Strictly speaking, N_{epi} should be scaled with $W_{SB}^{1/2}$ [4] to prevent a punch-through. In practice, however, the doping density of the lateral base region can be locally raised while keeping the N_{epi} unchanged, so that the vertical n-p-n transistors on the same wafer are not affected. The dependence of I_C with respect to α depends on X_{JE} and W_B. When W_B is much larger than the depletion width and X_{JE}, I_C increases with $1/\alpha$, but when W_B becomes smaller, I_C increases more rapidly than $1/\alpha$. Therefore, the decrease of τ_{SB} is stronger than that given by $1/\alpha^2$.

Since the lateral transistors are fabricated on the same chip with

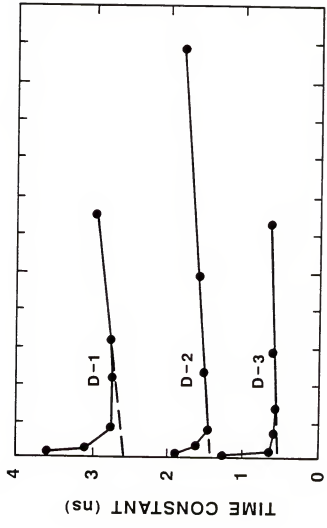

Figure 6.2 Emitter-collector time constant at different current levels. Device geometries are shown in Table 6.1.

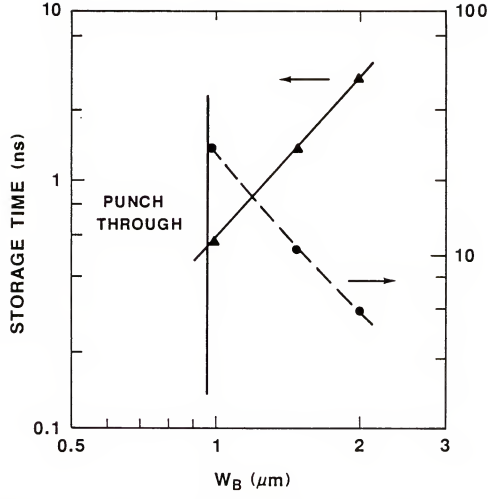

Figure 6.3 dependence of base charge storage time and current gain with the scaling in the lateral direction (D-1, D-2, and D-3).

the vertical n-p-n transistors, the vertical dimensions such as X_{epi}, X_{JE}, and epi layer doping concentration are not independent process parameters. Also the change of X_{JE} affects the lateral scaling because of lateral diffusion.

In this Section we discuss the vertical scaling and the effects of the changes in the vertical device profile. Fig. 6.4 displays the dependence of τ_{SB} and current gain on X_{JE} when the distance between the emitter-base and collector-base metallurgical junction is fixed to 0.8 μm and $X_{epi} - X_{JE} = 0.3$ μm and 0.5 μm, respectively. If we assume that the neutral base width at the surface is fixed by the design rules such that the punch-through does not occur, then the increase of X_{JE} will decrease the base current as we can see in (6.3). Also the collector current will increase according to (6.1).

For the understanding of τ_{SB} variations, we can separate the base charge into $Q_{B(I)}$ stored in region (I) and $Q_{B(s)}$ in the regions (II), (III), and (IV), and in the buried layer (Fig. 6.1). Then τ_{SB} can be expressed as follows

$$\tau_{SB} = \tau_{SB}^{(I)} + \tau_{SB}^{(s)} \quad , \tag{6.4}$$

where $\tau_{SB(I)} = Q_B^{(I)} / I_C$ and $\tau_{SB}^{(s)} = Q_B^{(s)} / I_C$. Since $Q_B^{(s)}$ does not change with X_{JE}, τ_{SB} becomes shorter when I_C gets larger. In contrast, $\tau_{SB}^{(I)}$ increases with X_{JE} due to the increased W_B^*. Thus, in the limit $X_{JE} \to 0$, $\tau_{SB} \approx \tau_{SB}^{(s)}$. As X_{JE} increases, τ_{SB} decreases and starts to increase after it reaches a minimum and $\tau_{SB} \approx \tau_{SB}^{(I)}$ at $X_{JE} \to \infty$.

Although there are many ways to scale the lateral p-n-p transistors, the present scaling of the lateral p-n-p transistors in the lateral dimension with the optimized structure in the vertical

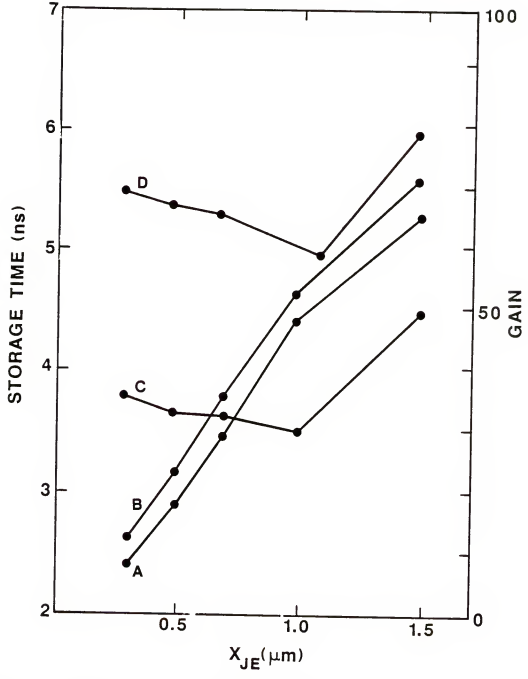

Figure 6.4 Dependence of the base charge storage time and the current gain with scaling in the vertical direction.
A: Current gain, $(X_{epi} - X_{JE}) = 0.3$ m.
B: Base charge storage time, $(X_{epi} - X_{JE}) = 0.3$ m.
C: Current gain, $(X_{epi} - X_{JE}) = 0.5$ m.
d: Base charge storage time, $(X_{epi} - X_{JE}) = 0.5$ m.

direction can be summarized as follows (assuming fixed N_{epi} and other doping concentrations):

(a) To minimize τ_{SB} the following relations are required

$$L = 1.5\ X_{JE} + W_{SB}^{(min)} + 2a \tag{6.5}$$

$$X_{epi} = X_{JE} + \Delta X_m \quad . \tag{6.6}$$

In (6.5), L is the length of the device in the lateral direction and $1.5X_{JE}$ accounts for the lateral diffusion of impurities, a is the minimum length determined by the design rule, $W_{SB}^{(min)}(N_{epi},a)$ is the minimum length between the emitter-base and collector-base metallurgical junction, and $\Delta X_m(N_{epi},N_{bl},BV_{CBO})$ is the allowed minimum distance between the collector-base metallurgical junction and the buried layer.

From (6.5) and (6.6), the optimized relations between the X_{epi} and L is established with X_{JE} as independent variable and all other parameters are fixed.

(b) X_{JE} is determined from Fig. 6.4 such as to maintain the required current gain and the optimum base charge storage time.

(c) After independent variable X_{JE} is determined, L and X_{epi} is determined from (6.5) and (6.6).

Fig. 6.5 displays the emitter-base time constant vs. the base current in the saturation mode (solid line) and its comparison with the emitter-collector time constant in the forward active mode (broken line) for the device D-1. It shows different behavior at high current level. The reason for the different behavior at high currents is that the quasi-neutral emitter region is in low injection and the base current is nearly proportional to $\exp(qV_{EB}/kT)$, while the base region

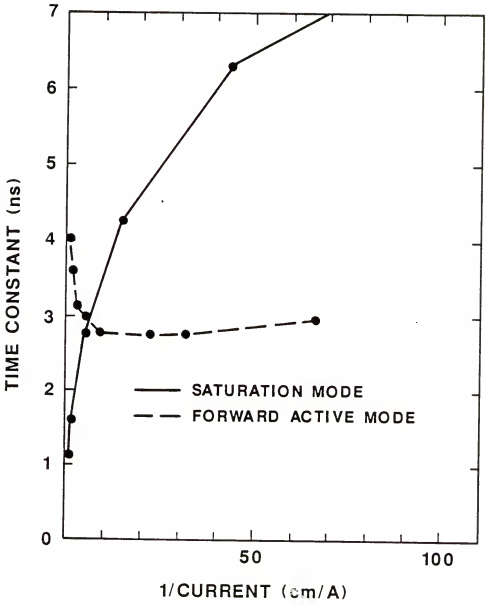

Figure 6.5 Comparison of emitter-collector time constant in the forward active mode with the emitter-base time constant in the saturation mode for D-1.

is in high injection. This can be seen in Fig. 6.6 which displays the Q_B/V_{EB} versus current for the forward active and saturation modes. Thus, the emitter-base time constant decreases monotonically.

As an attempt to decrease the base storage time, ion implantation was performed in device D-6 in the epi layer 0.1 μm below the emitter region with peak concentration of 10^{17} cm^{-3}, and vertical and lateral straggles of σ_x = 0.11 μm and σ_y = 0.085 μm, respectively. The simulated base charge storage time decreased to 190 ps from 230 ps for the device without ion implantation. The ion implantation decreases the concentration of minority holes, which reduces the stored charge under the horizontal emitter-base junction. The area of the active base region does not change as we can see from (6.1). In addition, the built-in electric field due to the implanted donor atoms accelerates the diffusion of holes and decreases the transit time. For the comparison we simulated the storage time when the ion implantation extends laterally to the collector. In this case τ_{SB} increased to 270 ps.

6.3 Summary

In this study we have investigated the characteristics of the lateral p-n-p transistors using FIELDAY program.

The simplified approximations for the collector and base current and the separation of minority hole charge inside the neutral base region led to the qualitative understanding of numerical results for the DC current gain and the base storage time. Based on this understanding, the procedure for the optimized scaling of the lateral p-n-p transistors was proposed and discussed.

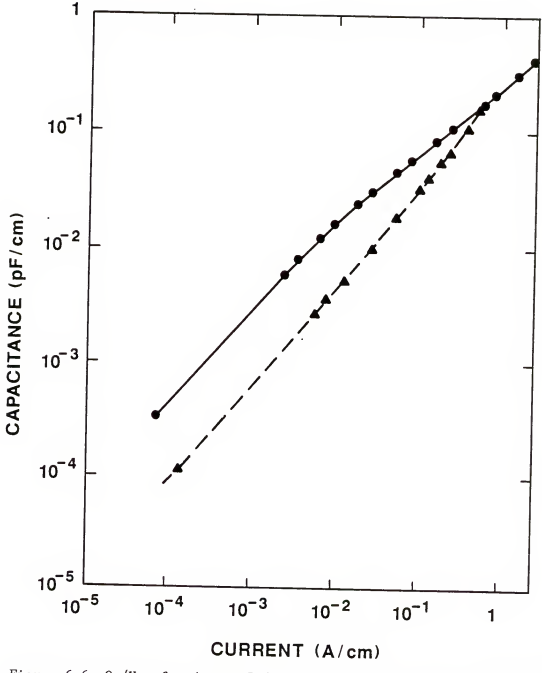

Figure 6.6 Q_B/V_{EB} for device D-1. Solid line is for the forward active mode and broken line is for the saturation mode.

CHAPTER SEVEN
SUMMARY

The major contributions of this study are

1) Development of the analytical solutions for the minority-carrier transport in the quasi-neutral region. This method is applied to the heavily-doped emitter region and a simple analytical approximation called quasi-neutral quasi-equilibrium approximation (QNQE) is derived, which is accurate for the modern bipolar transistors with polysilicon emitter contact.

2) Measurement of the bandgap narrowing by measuring the temperature dependence of the base current for the bipolar transistor with polysilicon emitter contact.

3) Measurement of the minority-hole diffusion length by comparing the base saturation current of the bipolar transistors with the same emitter doping profile but with different emitter contacts, ohmic contacts and the polysiliconcontacts.

4) A simple numerical method that can numerically simulate the small-signal minority-carrier transport in the quasi-neutral region was developed. High frequency behavior of the bipolar transistor due to the small-signal transport of the minority-carriers in the quasi-neutral region was studied numerically and interpreted physically.

5) Analytical solutions for the behavior of the space-charge region

in the high forward bias were developed by linearizing the Poisson equation, and compared with the numerical simulation results.

6) The DC and transient characteristics of the lateral p-n-p transistors were studied using the two dimensional device simulator. Based on that numerical study, a procedure for the optimized design of the lateral p-n-p transistors was developed.

APPENDIX A
SIMPLE ESTIMATION OF THE QUASI-NEUTRAL QUASI-EQUILIBRIUM CONDITION

The validity of the quasi-neutral quasi-equilibrium can be roughly estimated for a simple case. From (2.39), the second-order differential equation for $p'(x)/p_0(x)$ has the form

$$\frac{d^2U}{dX^2} + E_p' \frac{dU}{dx} + \frac{U}{L_p^2} = 0 \quad , \tag{A.1}$$

where

$$U(x) = p'(x)/p_o(x) = \exp(q\phi'/kT) \tag{A.2}$$

$$E_p' = \frac{d}{dx} \ln \left(\frac{D_p}{N_{Deff}}\right) \tag{A.3}$$

$$L_p^2 = D_p \tau_p \tag{A.4}$$

If we assume that E_p' and L_p are position independent, then (A.1) has the following general solution

$$U(x) = \exp(-E_p'x/2) \left[A \sinh \left[\beta(W_E - x)\right] + B \cosh \left[\beta (W_E - x)\right]\right] \tag{A.5}$$

where

$$\beta = \frac{1}{L_p} \left[1 + \frac{1}{4} E_p'^2 L_p^2\right]^{1/2} \quad . \tag{A.6}$$

Applying the boundary conditions at x = 0 and x = W_E expressed as

$$U(0) = 1 \tag{A.7}$$

$$\frac{d}{dx} \ln U\Big|_{x=W_E} = -\frac{S_p}{D_p} \tag{A.8}$$

we can calculate U(x).

$$U(x) = \exp(-E_p'x/2) \cdot \frac{\frac{1}{\beta}\left(\frac{S_p}{D_p} - \frac{E_p'}{2}\right)\sinh[\beta(W_E - x)] + \cosh[\beta(W_E - x)]}{\frac{1}{\beta}\left(\frac{S_p}{D_p} - \frac{E_p'}{2}\right)\sinh(\beta W_E) + \cosh(\beta W_E)} \tag{A.9}$$

Since the U(x) is a monotomically decreasing function of x, the quasi-wquilibrium condition can be expressed as

$$U(W_E) = \frac{\exp(-E_p'x/2)}{\frac{1}{\beta}\left(\frac{S_p}{D_p} - \frac{E_p'}{2}\right)\sinh(\beta W_E) + \cosh(\beta W_E)} \tag{A.10}$$

Fig. A.1 and A.2 displays the $U(W_E)$ versus S_p for $W_E = 0.2$ μm and for different values of L_p/W_E; $E_p' = \pm 1.5 * 10^5$ (1/cm) is the assumed appriximate normalized retarding or enhancing quasi-fields corresponding to $W_E \approx 0.2$ μm and $N_D(W_E) = 10^{20}$ cm^{-3} and $N_D(0) = 10^{18}$ cm^{-3}. As expected, a strong retarding field yields a nearly accurate quasi-equilibrium condition. Note that U = 1 signifies that the quasi-equilibrium condition is fully satisfied.

APPENDIX B
CALCULATION OF Q_E, C_E, AND τ_E FOR THE ZEROTH-ORDER APPROXIMATION

We derive here the Q_E, C_E, and τ_E for the zeroth order approximation.

From the continuity equation (2.12) we have

$$J_p(0) = q \int_0^{W_E} dx \frac{(p - p_0)}{\tau_p(x)} + J_p(W_E) \ . \tag{B.1}$$

This can be written in a charge-control representation as

$$\frac{Q_E}{\tau_E} = \frac{Q_E}{\tau_p} + \frac{Q_E}{\tau_t} \ , \tag{B.2}$$

where Q_E is the total excess hole charge stored in the (n-type) quasi-neutral emitter, τ_E is the charge-control emitter time constant, τ_p is a space-averaged hole lifetime, and τ_t is the transit time. In the zeroth-order approximation we obtain from (2.26), (2.27), and (2.29)

$$Q_E = [\exp (qV_{BE}/kT) - 1] \int_0^{W_E} qp_0(x) \, dx \tag{B.3}$$

$$\tau_t = \frac{1}{S_p p_0(W_E)} + \int_0^{W_E} p_0(x) \, dx \tag{B.4}$$

$$\tau_p = \frac{\int_0^{W_E} p_0(x)\ dx}{\int_0^{W_E} \frac{p_0(x)}{\tau_p(x)}\ dx} \quad . \tag{B.5}$$

The quasi-static emitter capacitance is $C_E = dQ_E/dV_{BE} \approx (q/kT)Q_E$. A large signal dynamic circuit model for the emitter consists of C_E in parallel with the controled current source implied by (2.29), connected between the intrinsic emitter and base terminals. From this one can calculate, for example, the quasi-static approximation of the propagation delay contributed by the excess charge in the emitter.

REFERENCES

1. W. Shockley, "Theory of p-n junctions in semiconductors and p-n junction transistors," Bell Syst. Tech. J., vol. 28, pp. 435-489, 1949.

2. K. Okada, K. Aomura, T. Nakamura, and H. Shiba, "A new polysilicon process for bipolar device-PSA technology," IEEE Trans. Electron Devices, vol. ED-26, p. 385, April 1979.

3. P. M. Solomon, and D.D. Tang, "Bipolar circuit scaling," IEEE ISSCC, Dig. Tech. Papers, pp. 86-87, 1979.

4. D. D. Tang and P.M. Solomon, "Bipolar transistor design for optimized power-delay logic circuits," IEEE J. Solid-State Circuits, vol. SC-14, pp. 679-684, August 1979.

5. J. Graul, A. Glasl, and M. Murman, "High performance transistors with arsenic-implanted polysil emitters," IEEE J. Solid-State Circuits, vol. Sc-11, pp. 491-494, August 1976.

6. T. H. Ning, and R. D. Issac, "Effect of emitter contact on current gain of silicon bipolar devices," IEEE Trans. Electron Devices, vol. ED-27, pp. 2051-2055, November 1980.

7. A. Neugroschel, M. Arienzo, Y. Komen, and R. D. Issac, "Experimental study of the minority-carrier transport at the polysilicon-monosilicon interface," IEEE Trans. Electron Devices, vol. ED-32, pp. 807-816, April 1985.

8. W. P. Dumke, "Minority carrier injection into a heavily doped emitter. Approximate solution for Auger Recombination," Solid-State Electron., vol. 24, pp. 155-157, Feburary 1981.

9. H. C. de Graaf J. W. Slotboom, and A. Schmitz, "The emitter efficiency of bipolar transistors," Solid-State Electron., vol. 20, pp. 515-521, June 1977.

10. R. Amantea, "A new solution for minority carrier injection into the emitter of bipolar transistor," IEEE Trans. Electron Devices, vol. ED-27, pp. 1231-1238, July 1980.

11. M. A. Shibib, F. A. Lindholm, and F. Therez, "Heavily doped transparent emitter regions in junction solar cells, diodes, and transistors," IEEE Trans. Electron Devices, vol. ED-26, pp, 959-965, June 1979.

12. J. G. Fossum and M. A. Shibib, "An analytical model for minority carrier transport in heavily doped regions of silicon devices," IEEE Trans. Electron Devices, vol. ED-28, pp. 1018-1025, September 1981.

13. C. R. Selvakumar, "Simple general analytical solution to the minority carrier transport in heavily doped semiconductors," J. Appl. Phys., vol. 56, pp. 3476-3478, December 1984.

14. J. del Alamo and R. M. Swanson, "The physics and modeling of heavily doped emitters," IEEE Trans. Electron devices, vol. ED-31, pp. 1878-1888, December 1984.

15. E. de Castro and M. Rudan, "Integral-equation solution of minority carrier transport problems in heavily doped semiconductors," IEEE Trans. Electron Devices, vol. ED-31, pp. 785-793, June 1984.

16. A. H. Marshak, M. A. Shibib, J. G. Fossum and F. A. Lindholm, "Rigid band analysis of heavily doped semiconductors," IEEE Trans. Electron Devices, vol. ED-28, pp. 293-298, March 1981.

17. H. J. J. Deman, "The influence of heavy doping on the emitter efficiency of bipolar transistor," IEEE Trans. Electron Devices, vol. ED-18, pp. 833-835, October 1971.

18. J. W. Slotboom and H. C. de Graff, "measurements of bandgap narrowing in Si bipolar transistors," Solid State Electron., vol. 19, pp. 857-862, October 1976.

19. N. D. Arora, J. R. Hauser, and D. J. Roulston, "Electron and hole mobilities in silicon as afunction of concentration and temperature," IEEE trans. Electron Devices, vol. ED-29, pp. 292-295, February 1982.

20. R. W. Keyes, "density of states of degenerate n-type silicon from elastic constants," Solid State Comm., vol. 32, pp. 179-180, 1979.

21. J. Dziewior and W. Schmid, "Auger coefficients for highly doped and highly excited silicon," Appl. Phys. Lett., vol. 31, pp. 346-348, September, 1977.

22. D. S. Lee, "Physical analysis of doping dependence of carrier lifetime in degenerate and nondegenerate silicon," Ph.D. dissertation, University of Florida, 1982.

23. J. del Alamo, S. Swirhun, and R. M. Swanson, "Measuring and modeling minority carrier transport in heavily doped silicon," Solid-State Elecreon., vol. 28, pp. 47-54, January 1985.

24. D. D. Tang, "Heavy doping effects in n-p-n bipolar transistors," IEEE trans. Electron Devices, vol. ED-27, pp. 563-570, March 1980.

25. A. W. Wieder, "Emitter effects in shalloe bipolar devices: Measurement and consequences," IEEE Trans Electron Devices, vol. ED-27, pp. 1402-1408, August 1980.

26. G. E. Possin, M. S. Adler, and B. J. Baliga, "Measurement of p-n product in heavily doped epitaxial emitters," IEEE Trans Electron devices, vol. ED-31, pp. 3-17, January 1984.

27. A. Neugroschel and F. A. Lindholm, "Evidence for low diffusivity and mobility of minority carriers in highly doped Si and interpretation ," Appl. Phys. Lett., vol. 42, pp. 176-178, 1983.

28. H. S. Bennett, " Hole and electron mobilities in heavily doped silicon: comparison of theory and experiment." Solid-State Electron., vol. 26, pp. 1157-1166, 1983.

29. A. Neugroschel, S.C. Pao, and F. A. Lindholm, "Method for determining energy gap narrowing in highly doped semiconductors," IEEE Trans. Electron devices, vol. ED-29, pp. 894-902, May 1982.

30. G. G. Macfarlane, J. P. Mclean, J. E. Quarington, and V. Roberts, "Fine structure in the absorption-edge spectrum of Si," Phys. Rev., vol. 3, pp. 1245-1254, 1958.

31. J. Wagner, "Photoluminiscence and excitation spectroscopy in heavily doped n- and p-type silicon," Phys. Rev. B, vol. 29, pp. 2002-2009, 1984.

32. J. Wagner, To be published.

33. M. Balkanski, A. Aziza, and E. Amzallag, "Infrared absorption in heavily doped n-type Si," Phys. Status Solidi, vol. 31, pp. 323-330, 1969.

34. A. Neugroschel, M. Arienzo, Y. Komen, and R. D. Issac, "Experimental study of the minority-carrier transport at the polysilicon-monosilicon interface," IEEE trans. Electron Devices, vol. ED-32, pp. 817-825, April 1985.

35. T. H. Ning and R. D. Issac, "Effect of emitter contact on current gain of silicon bipolar devices," IEEE Trans. Electron Devices, vol. ED-27, pp. 2501-2505, November 1980.

36. Z. Yu, B. Ricco, and R. W. Dutton, "A Comprehensive analytical and numerical model of polysilicon emitter contacts in bipolar transistors," IEEE Trans. Electron Devices, vol. ED-31, pp. 773-784, June 1984.

37. D. B. Jackson and C. T. Sah, "Thermally generated electron traps in boron-implanted, phosporous-doped silicon," J. Appl. Phys. vol. 58(B), pp. 2225-2229, 1985.

38. B. Benna, T. Meister, H. Schaber and A. W. Wieder, "Base current analysis of poly-Si emitter bipolar transistors," IEDM Tech. Dig., pp. 302-305, 1985.

39. B. V. Gokhale, "Numerical solutions for a one-dimensional silicon n-p-n transistor," IEEE Trans. Electron Devices, vol. ED-17, pp. 594-602, August 1970.

40. M. Kurata, "A small signal transistor for one-dimensional transistors," IEEE Trans. Electron Devices, vol. ED-18, pp. 200-210, March 1971.

41. S. E. Laux, "Techniques for small-signal analys of semiconductor devices," IEEE Trans. Electron Devices, vol. ED-32, pp. 2028-2037, October 1985.

42. B. R. Chawla and H. K. Gummel, "Transition region capacitance of diffused p-n junctions," IEEE Trans. Electron Devices, vol. ED-18, pp. 178-195, March 1971

43. D. E. Burk and V. de La Torre, "An empirical fit to minority hole mobilities," IEEE Electron Device Lett., pp. 231-233, July 1984.

44. F. N. Gonzalez and A. Neugroschel," Measuremant of diffusion length, lifetime, and surface recombination velocity in the semiconductor devices," IEEE Trans. Electron Devices, vol. ED-31, pp. 413-416, April 1984.

45. A. Neugroschel, "Minority -carrier diffusion coefficients and mobilities in silicon," IEEE Electron Device Lett., vol. EDL-6, pp. 425-427, August 1985.

46. A. Neugroschel, B. Y. Hwang, and J. S. Park, "Transit time and charge storage measurements in heavily doped emitters," IEEE Electron Device Lett., pp. 83-85, February 1986.

47. A. van der Ziel, Solid State Physical Electronics, Prentice Hall Inc., 1976.

48. C. T. Sah, "The Equivalent Circuit Model in Solid-State Electronics-III," Solid State Electron., vol. 13, pp. 1547-1575, 1970.

49. M. K. Chen, "Inclusion of quasi-neutral region delay in quasi-static diode analysis," University of Florida, Master Thesis, 1986.

50. J. L. Moll, Physics of Semiconductors, New York, McGraw-Hill, Chapter 7, 1964.

51. C. T. Sah, "Effects of electrons and holes on the transition layer characteristics of linearly graded p-n junction," Proc. IRE, vol. 49, pp. 603-618, March 1961.

52. D. P. Kennedy and R. R. O'Brien, "On the mathematical theory of

the linearly-graded p-n junction," IBM J. Res. Develop., pp. 252-270, May 1967.

53. Y. F. Chang, "The capacitances of p-n junctions," Solid-State Electron., vol. 10, pp. 281-287, April 1967

54. R. M. Sisri and A. R. Boothroyd, "Characterization of space-charge properties of a linearly graded junction by approximate regional analysis method," IEEE Trans. Electron Devices, vol. ED-23, pp. 348-353, March 1976.

55. H. Guckel, D. Thomas, S. Iyengar and A. Demirkol, "Transition region behavior in abrupt, forward biased p-n junctions," Solid-State Electron., vol. 20, pp. 647-652, July 1977.

56. S. C. Rustiyagi and S. K. Chattopadhyaya "Characterization of linearly-graded junctions,: Solid-State Electron., vol. 22, pp. 819-827, September 1979.

57. K. Lee and R. M. Warner, Jr., "Modeling the transition region of a symmetric step junction," Solid-State Electron., vol. 25, pp. 115-118, Feburary 1982.

58 R. M. Warner, Jr. and R. P. Jindal, "Replacing the depletion approximation ," Solid-State Electron., vol. 26, pp. 335-342, April 1983.

59. S. P. Morgan and F. M. Smits, "Potential distribution and capacitance of graded p-n junction," Bell Syst. Tech. J., vol. 39, pp. 1573-1602, November 1960.

60. F. A. Lindholm, "Simple phenomenological modeling of transition-region capacitance of forward-biased p-n junction diode and transistor devices," J. Appl. Phys., vol. 53(11), pp. 7606-7608, November 1982.

61. J. H. van den Biesen, "p-n junction capacitances part I: The depletion capacitances," Phillips J. Res. 40, pp. 88-102, 1985.

62. J. H. van den Biesen, " p-n junction capacitances part II: The neutral capacitances," Phillips J. Res., 40, pp. 103-113, 1985.

63. R. B. Shirts and Gordon, "Improved approximate analytic charge distributions for abrupt p-n junctions," J. Appl. Phys., vol. 50(4), pp. 2840-2847, April 1979

64. A. M. Marshak and K. M. van Vliet, "On the separation of quasi-Fermi levels and the boundary conditions for junction devices," Solid-State Electron., vol. 23, pp. 1223-1228, December 1980.

65. A. van der Ziel, "Boundary conditions for forward biased p-n junctions," Solid-State Electron., vol. 16, pp. 1509-1511, December 1973

66. N. W. Ashcroft and N. D. Mermin, Solid State Physics, Holt, Rinehart and Winston, 1976.

67. E. M. Buturla, P. E. Cottrell, B. M. Grossman, K. Salsburg, "Finite-element analysis of the semiconductor analysis: The FIELDAY program," IBM J. Res. Develop. vol. 25, pp. 218-231, 1981.

68. K. S. Seo and C. K. Kim, "On the geometrical factor of lateral p-n-p transistors," IEEE Trans. Electron Devices, vol. ED-27, pp. 295-297, 1980.

69. H. K. Gummel and H. C. Poon, "An integral charge control model of bipolar transistors," Bell Syst. Tech. J., p. 827, 1970

BIOGRAPHICAL SKETCH

Jong-Sik Park was born in Seoul, Korea, on September 6, 1953. He received the B.S. degree in physics from Seoul National University in 1976 and M.S. degree in physics from Korea Advanced Institute of Science and Technology, Korea, in 1978. Since September 1984, he has been working toward the Ph.D. degree in electrical engineering at the University of Florida, Gainesville.

From 1978 to 1981 he was a full-time lecturer at the Department of Electronics, Daegu, Korea.

From 1981 to 1984 he was a graduate student in the department of Physics, University of Florida, where he did research on the solid hydrogen and nuclear magnetic resonance.

During the summer of 1986 he was employed by the IBM Thomas J. Watson research Center.

His area of interest includes high speed semiconductor device modeling and characterization.

I certify that I have read this study and that in my opinion it conforms to acceptable standards of scholary presentation and is fully adequate, in scope and quality, as a dissertation for the degree of Doctor of Philosophy.

Arnost Neugroschel, Chairman
Professor of Electrical Engineering

I certify that I have read this study and that in my opinion it conforms to acceptable standards of scholary presentation and is fully adequate, in scope and quality, as a dissertation for the degree of Doctor of Philosophy.

Fredrik A. Lindholm, Cochairman
Professor of Electrical Engineering

I certify that I have read this study and that in my opinion it conforms to acceptable standards of scholary presentation and is fully adequate, in scope and quality, as a dissertation for the degree of Doctor of Philosophy.

Sheng S. Li
Professor of Electrical Engineering

I certify that I have read this study and that in my opinion it conforms to acceptable standards of scholary presentation and is fully adequate, in scope and quality, as a dissertation for the degree of Doctor of Philosophy.

Gys Bosman
Assistant Professor of Electrical Engineering

I certify that I have read this study and that in my opinion it confirms to acceptable standards of scholary presentation and is fully adequate, in scope and quality, as a dissertation for the degree of Doctor of Philosophy.

Hendrik Jan Monkhorst
Professor of physics

This dissertation was submitted to yhe Graduate Faculty of the College of Engineering and to the Graduate School and was accepted as partial fulfillment of the requirements for the degree of Doctor of Philosophy.

May 1987

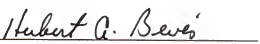

Dean, College of Engineering

Dean, Graduate School